Coupling between Walker and Hadley circulations mediated by low cloud feedback

Rolf Schimmer,[a,b] Sarah M. Kang[a]

[a] *Max Planck Institute for Meteorology, Bundesstraße 53, 20146 Hamburg, Germany.*

[b] *International Max Planck Research School on Earth System Modelling, Bundesstraße 53, 20146 Hamburg, Germany.*

Corresponding author: Rolf Schimmer, rolf.schimmer@mpimet.mpg.de

ABSTRACT

The tropical Pacific hosts the primary region of deep convection and forms the shared ascending branch of the Walker and Hadley circulations, which regulate the distribution of energy, angular momentum, and moisture across the climate system. Despite their importance and spatial entanglement, the dynamical coupling between these two circulations remains poorly understood. Here we show that the Walker and Hadley circulations are intrinsically linked by cloud radiative feedbacks. Using an idealized aquaplanet slab-ocean configuration, we introduce a Walker circulation of varying strength by altering the amplitude of prescribed zonally antisymmetric surface heat flux. The Hadley circulation remains largely insensitive to weak Walker circulation forcing, but weakens strongly once the forcing exceeds a critical threshold. This regime transition occurs when cold-patch cooling becomes sufficiently strong to trigger a positive low-cloud feedback. Once triggered, this feedback induces substantial equatorial cooling and lowers the threshold for deep convection in the off-equatorial tropics, thereby reorganizing tropical convection meridionally. Cloud-locked simulations confirm the key role of cloud radiative feedbacks in controlling this transition. We further show that the low-cloud feedback is driven primarily by local cooling over the cold patch, rather than by remote warming over the warm patch. These results suggest that eastern Pacific low-cloud feedbacks are a key control on tropical convective organization – offering an alternative conceptual view of tropical Pacific atmospheric dynamics in which the eastern Pacific cold tongue plays an active role in organizing tropical convection and mediates the interactions between the Walker and Hadley circulations.

SIGNIFICANCE STATEMENT

We want to understand the intrinsic link between the Walker and the Hadley circulation which represent the two most important large-scale overturing circulations of the tropical atmosphere. This is important because their shared ascending branch in the western Pacific forms the main source of deep convection regulating the distribution of energy, angular momentum, and moisture across the climate system. Our results provide a theory on how the two circulations are linked by cloud radiative effects of low clouds and suggest that the eastern Pacific plays an active and more important role in organizing tropical convection than commonly assumed.

1. Introduction

The Pacific Ocean plays a pivotal role in Earth's climate, as it hosts the primary region of deep convection that forms the ascending branch of both the zonally symmetric Hadley circulation (HC) and the zonally asymmetric Walker circulation (WC). The HC is characterized by ascent in the equatorial region and descent in the subtropics, governed by energy and angular momentum constraints (Held and Hou 1980, Neelin and Held 1987). It plays an important role in the global climate system by importing moisture into the tropics and exporting energy and angular momentum poleward (Hu et al. 2018). Consequently, many large-scale features of the climate system are closely linked to the Hadley circulation, such as monsoon systems, jet streams, and the location of storm tracks (Bordoni and Schneider 2008, Korty and Schneider 2008, Trenberth and Stepaniak 2003). In contrast, the Walker circulation features strong ascent over the western Pacific and descent over the eastern equatorial Pacific, and is commonly understood to be driven by the zonal sea surface temperature (SST) gradient (Bjerknes 1969). Because this gradient is strongly modulated by the El Niño-Southern Oscillation (ENSO), the WC exhibits pronounced interannual variability. Through associated atmospheric teleconnections, including Rossby wave propagation, it strongly affects precipitation patterns in both the tropics and the extratropics (Barichivich et al. 2018, Kosaka and Xie 2013, Bayr et al. 2014). Given that the HC and WC share an ascending branch over the Maritime Continent in the western Pacific, and that the Western Pacific warm pool is often thought to exert a dominant control on tropical convective patterns by setting the free tropospheric temperature gradient (Andrews and Webb 2018, Dong et al. 2019, Zhang and Fueglistaler 2020), one might expect the two circulations to be dynamically coupled. However, the nature of this coupling remains poorly understood, and no established theoretical framework yet exists to explain how these two circulation systems interact.

The WC is largely controlled by the zonal SST gradient (Wills et al. 2017), whereas the HC is linked to meridional SST gradients (Feng et al. 2016). If the two circulations are dynamically linked, this linkage may therefore be reflected in a relationship between the zonal and meridional SST gradients. Such covariability is supported by paleoclimatic evidence. For example, Fedorov et al. (2015) show that zonal and meridional SST gradients are tightly linked over the past five million years, through the wind-driven subtropical ocean cell. A weakened meridional SST gradient, driven by subtropical ocean warming, reduces upper-ocean stratification in the eastern equatorial Pacific via the ocean tunnel mechanism, leading to SST warming there and a weakened zonal SST gradient. Thus, one might expect the WC and HC to covary on long time scales due to the link between zonal and meridional SST gradients.

A similar relationship between zonal and meridional SST gradients is found in slab ocean simulations, indicating that atmospheric processes alone can also produce such covariability (Hwang et al. 2017; Kang et al. 2020). In response to prescribed Southern Ocean cooling, the inter-hemispheric SST gradient increases, strengthening the southern HC. At the same time, Southern Ocean cooling induces pronounced cooling in the eastern equatorial Pacific through wind-evaporation-SST feedback and shortwave cloud feedbacks (Kim et al. 2022), thereby enhancing the zonal SST gradient and strengthening the WC. This Southern Ocean-driven covariability between the meridional and zonal SST gradients also exists in coupled atmosphere-ocean simulations (Kang et al. 2020). By contrast, the response to northern extratropical cooling is more complex and depends on timescale (Kang et al. 2020; Tseng and Hwang 2024).

On interannual timescales, the HC and WC are anticorrelated in association with ENSO variability (Minobe 2004, Ma and Li, 2008, Bayr et al., 2014, Guo and Tan, 2018). During El Niño events, the WC weakens in response to a reduced zonal SST gradient across the equatorial Pacific, while the HC strengthens in response to enhanced equatorial heating (Lu et al. 2008). A similar anticorrelation also characterizes recent multidecadal trends. Over recent decades, the WC has been observed to strengthen associated with an enhanced zonal SST gradient in the equatorial Pacific, linked to eastern-basin cooling (Watanabe et al. 2023; Kang et al. 2025). Meanwhile, the HC has been suggested to weaken, particularly in the Northern Hemisphere (Chemke and Yuval 2023). In contrast, under CO2 forcing, most climate models project a weakening of both the WC and HC on quasi-equilibrated timescales, implying that the changes in HC and WC may instead become positively correlated in the long-term CO2-forced response.

Taken together, these studies suggest that the sign of HC-WC covariability depends on both the timescale and the nature of the perturbation. It remains unclear whether there is an intrinsic dynamical relationship between the two circulations, and we still lack a fundamental understanding of HC-WC coupling. As a first step toward addressing this gap, this study examines how changes in the WC influence the HC. We address this question using an idealized aquaplanet configuration coupled to a slab ocean model, in which the WC strength can be systematically altered by prescribing zonally antisymmetric surface heat fluxes of varying amplitude in the equatorial region. Such idealized configurations have been widely used to establish physical frameworks for understanding changes in either the WC (Merlis and Schneider 2011, Feldl et al. 2014, Wills et al. 2017) or the HC (Kang et al. 2008, Feldl and Bordoni 2016, Kim et al 2022). Yet, none has explicitly examined the dynamical linkage between the two circulation systems. Our goal therefore is to understand how a change in WC strength projects onto the HC, as our experiment setup allows us to isolate the atmospheric response to changes in WC-like zonal overturning.

A detailed description of the experimental setup is provided in Section 2. In Section 3, we introduce an energetic framework that decomposes the vertically integrated moist static energy budget into zonal and meridional components, allowing the WC and HC responses to be diagnosed separately. In Section 4, we use this framework to show how cloud radiative feedbacks mediate the HC-WC coupling, and how changes in the WC project onto the HC through a meridional reorganization of convection governed by convective instability. We discuss the broader implications of these findings and conclude in Section 5.

2. Experimental Setup

We employ the ECHAM6 atmospheric model coupled to a 10m deep aquaplanet slab ocean (Stevens et al. 2013). The simulations are performed at T63 horizontal resolution, roughly corresponding to a 2° grid spacing, with 47 vertical layers. Solar radiation is prescribed at equinox, without any seasonal or diurnal cycle. The slab ocean provides a convenient framework for controlling the strength of the Walker circulation by prescribing a zonally antisymmetric surface heat flux. Following Merlis and Schneider (2011), the zonally antisymmetric component of the prescribed heat flux is given by

$$Q_{\mathrm{WC}}(\lambda, \phi) = Q_1 \exp\left(-\frac{(\lambda - \lambda_W)^2}{\lambda_1^2} - \frac{\phi^2}{\phi_1^2}\right) - Q_1 \exp\left(-\frac{(\lambda - \lambda_E)^2}{\lambda_1^2} - \frac{\phi^2}{\phi_1^2}\right) \tag{1}$$

where $\lambda_{\mathrm{W}} = 120°$ and $\lambda_{\mathrm{E}} = 270°$ are the center of the warm and cold patches, respectively, and $\lambda_1 = 30°$ and $\phi_1 = 7°$ are the zonal and the meridional extent of each patch (Fig. 1a). The distance $\Delta\lambda = \lambda_E - \lambda_W$ between the two patches is chosen to roughly mimic the longitudinal extent between the maritime continent and the cold tongue in the tropical Pacific, following Feldl et al. (2014). The WC strength is varied by altering Q_1 from 0 to 100 $\mathrm{W\,m^{-2}}$ in increments of 10 $\mathrm{W\,m^{-2}}$. ERA5 reanalysis data (Hersbach et al. 2020) show that the zonal gradient of surface heat flux across the tropical Pacific is approximately 90 $\mathrm{W\,m^{-2}}$ (Fig. S1), which falls well within our experimental range of 0 – 200 W m^{-2}. The sign convention for the heat flux is defined as positive upward. Accordingly, positive values of Q_{WC} produce a warm patch in the western basin, while negative values produce a cold patch in the eastern basin.

In addition, we prescribe a zonally symmetric surface heat flux to mimic the effect of poleward ocean heat transport; without this term, the HC would be unrealistically strong. This zonally symmetric heat flux is prescribed as follows:

$$Q_{\mathrm{HC}}(\lambda, \phi) = -Q_0 \left(\frac{\phi_0^2 - 2\phi^2}{\phi_0^2} \right) \exp\left(-\frac{\phi^2}{\phi_0^2} \right) \tag{2}$$

where $\phi_0 = 16°$ sets the meridional extent and $Q_0 = 50$ W m^{-2} controls the amplitude. The choice of Q_0 follows previous studies (Bordoni and Schneider 2008, Merlis and Schneider 2011, Wills et al 2017). We consider $Q_1 = 80$ W m^{-2} as the most realistic case where the resulting HC strength, measured by the maximum zonally averaged mass streamfunction, is $\psi_{500} = 135 \cdot 10^9$ kg s^{-1}, comparable to the annual-mean Hadley circulation based on ERA5 reanalysis data. While $Q_1 = 50$ W m^{-2} better approximates the observed zonal gradient in surface heat flux, it results in an overestimation of Hadley circulation strength. The same zonally symmetric flux Q_{HC} is prescribed in all cases with varying Q_{WC}.

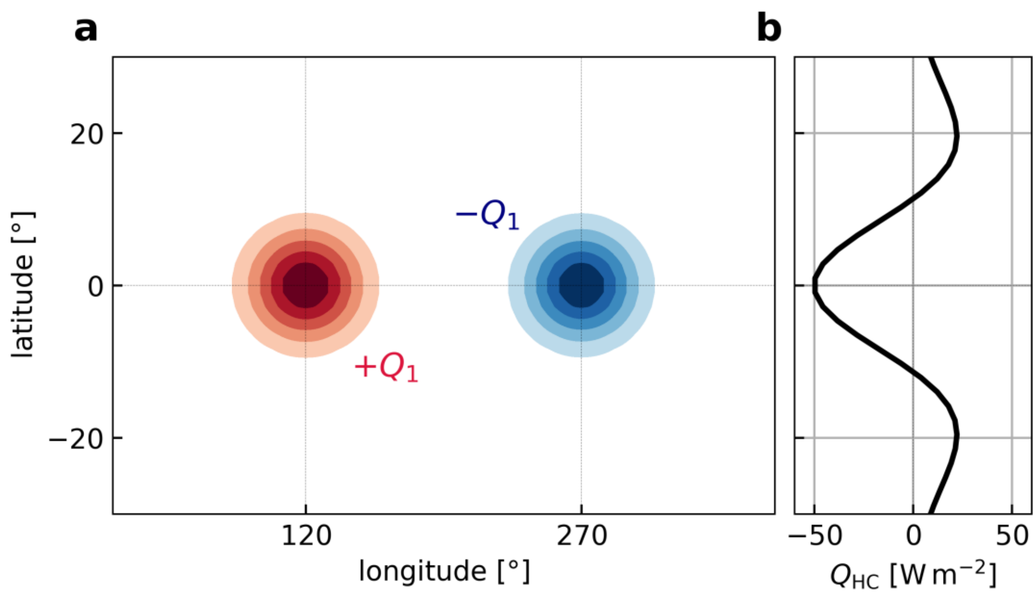

Fig. 1. Prescribed surface heat flux $Q = Q_{WC} + Q_{HC}$ as given by the sum of (a) the zonally antisymmetric flux Q_{WC} ranging in amplitude between $Q_1 = [0\ldots100]$ W m^{-2} and (b) the

zonally symmetric flux Q_{HC} with a fixed amplitude of $Q_0 = 50\ \mathrm{W\ m^{-2}}$. Positive values indicate heating of the surface and negative values indicate cooling of the surface.

All experiments are spun up for 5 years, and the subsequent 10 years are used for the analysis. Because the system is hemispherically symmetric by construction, we base our analysis on the average between the two hemispheres, which effectively doubles the sample size. Anomalies relative to the control case ($Q_1 = 0$) are denoted by δ. In Section 4.4, we repeat the same set of experiments with cloud radiative effects (CRE) inhibited. This is achieved by writing out cloud water, cloud ice, and cloud cover from the control run at each radiation time step (two-hourly) and prescribing these fields in the perturbed runs with nonzero Q_1. The cloud fields are prescribed only within the radiation scheme, while their dynamical and microphysical evolution remains interactive. This approach effectively suppresses cloud radiative effects. The implementation in ECHAM6 follows Voigt and Shaw (2015).

3. Experimental Setup

a. Decomposing the MSE budget

Consider the moist static energy (MSE) budget in its vertically integrated form (Neelin and Held 1987):

$$\partial_t \langle c_p T + L_v q \rangle + \langle \mathbf{u} \cdot \boldsymbol{\nabla}\big(c_p T + L_v q\big) \rangle + \langle \omega\, \partial_p h \rangle = F_{\mathrm{net}} \tag{3}$$

where brackets indicate a mass-weighted vertical integral. F_{net} is the net energetic input into the atmospheric column, $\mathbf{u}$ is the horizontal wind vector, ω is the vertical pressure velocity and *h* is the moist static energy, defined as $h = c_p T + \Phi + L_v q$, with Φ being the geopotential, $c_p T$ the internal energy and $L_v q$ the latent heat. The net energetic input F_{net} is the sum of the upward surface heat flux (denoted by Q) and the downward top-of-atmosphere (TOA) radiative fluxes (denoted by F_{TOA}): $F_{\mathrm{net}} = Q + F_{\mathrm{TOA}}$. The TOA radiative flux can be further decomposed into cloud and clear-sky components: $F_{\mathrm{TOA}} = F_{\mathrm{cld}} + F_{\mathrm{clr}}$ where F_{cld} denotes the cloud-radiative component and F_{clr} denotes the clear-sky component.

The time-mean vertically integrated MSE budget then yields

$$\langle \overline{\mathbf{u}} \cdot \boldsymbol{\nabla}\big(c_p \overline{T} + L_v \overline{q}\big) \rangle + \langle \overline{\omega}\, \partial_p \overline{h} \rangle + R = \overline{F}_{\mathrm{net}} \tag{4}$$

where an overbar denotes the time mean and the residual Rrepresents the transient eddy contribution. To obtain separate energetic constraints for the zonal and meridional components, which respectively represent the WC and HC, we decompose F_{net} using the energy flux potential following Boos and Korty (2016). The energetic flux potential is computed by solving the inverse Poisson's approach of the form $\nabla^2\chi \equiv F_{\mathrm{net}}$, where χ is a scalar potential with arbitrary additive constant. Building on the vertically integrated MSE budget (Neelin and Held 1987),

$$\boldsymbol{\nabla} \cdot \langle \mathbf{u}h \rangle = F_{\mathrm{net}}, \tag{5}$$

the divergent component of the horizontal MSE flux can be written as the gradient of this potential:

$$\boldsymbol{\nabla}\chi = \langle \mathbf{u}h \rangle_{\mathrm{div}} = \begin{pmatrix} \langle uh \rangle \\ \langle vh \rangle \end{pmatrix}_{\mathrm{div}}. \tag{6}$$

This formulation allows the zonal and meridional components of the MSE flux to be associated with their corresponding contributions to the net energy input. Taking the divergence of each component separately yields

$$\partial_\lambda \langle uh \rangle_{div} + \partial_\phi \langle vh \rangle_{div} = F_{\mathrm{net},\lambda} + F_{\mathrm{net},\phi}. \tag{7}$$

where $F_{\mathrm{net},\lambda}$ and $F_{\mathrm{net},\phi}$ denote the energetic inputs associated with zonal and meridional MSE transport, respectively.

We now partition the three-dimensional flow into zonal and meridional components, corresponding to the Walker and Hadley circulations, respectively, following the method introduced by Schwendike et al. (2014). Assuming non-rotational flow, the mass continuity equation is satisfied independently for the zonal and meridional components:

$$\frac{1}{a}\frac{\partial}{\partial\lambda}u_{\mathrm{div}} + \frac{\partial}{\partial p}(\omega_\lambda \cos\phi) = 0 \tag{8a}$$

$$\frac{1}{a}\frac{\partial}{\partial\phi}(v_{\mathrm{div}} \cos\phi) + \frac{\partial}{\partial p}(\omega_\phi \cos\phi) = 0, \tag{8b}$$

where u_{div} and v_{div} denote the divergent components of the zonal and meridional winds, respectively. This leads to a decomposition of the vertical velocity into $\omega = \omega_\lambda + \omega_\phi$. We associate the Walker circulation with the zonal component of vertical motion ω_λ, and the Hadley circulation with the meridional component, ω_ϕ. Figure 2 shows that a substantial fraction of the zonal contrast in total vertical motion (solid) arises from the meridional component, ω_ϕ (dotted), rather than from the Walker-like zonal component ω_λ (dashed). Hence, the zonal contrast in total vertical motion can be misleading as a measure of WC strength. We therefore define the Walker circulation strength as the warm-patch average of $\omega_{500,\lambda}$. The Hadley circulation strength is defined as the zonal mean of $\omega_{500,\phi}$, averaged over the equatorial band $\phi \leq \pm 5°$. By construction, this metric is equivalent to the zonal mean of the total vertical velocity, because $\omega_{500,\lambda}$ has no zonal-mean contribution

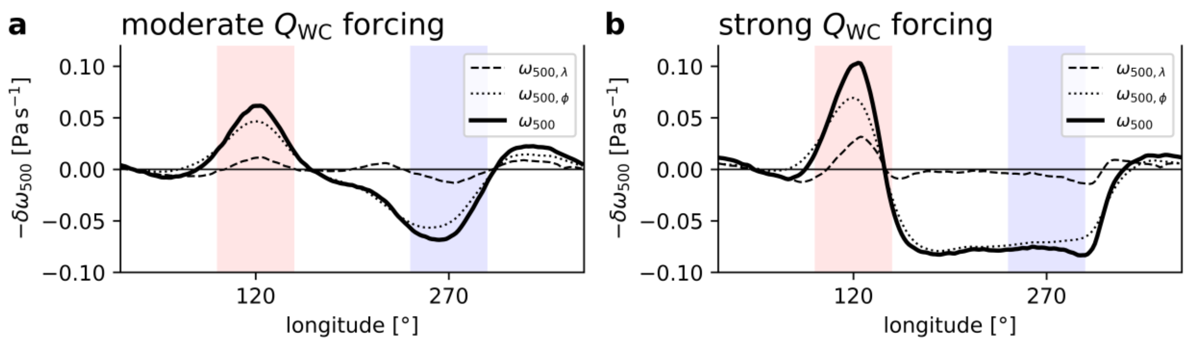

Fig. 2. Example of the mid-tropospheric vertical velocity anomaly $\delta\omega_{500}$ (solid) decomposed into the zonal component $\delta\omega_{500,\lambda}$ (dashed) and the meridional component $\delta\omega_{500,\phi}$ (dotted) for (a) a moderate Q_{WC} forcing scenario with $Q_1 = 60\ \text{W m}^{-2}$ and (b) a strong Q_{WC} forcing scenario with $Q_1 = 100\ \text{W m}^{-2}$. Red and blue shading indicates the locations of the warm and cold patches, respectively.

Eqs. (7) and (8) provide the two ingredients needed to decompose the time-mean MSE budget in Eq. (4). Eq. (7) partitions the net energy input into the components associated with zonal and meridional MSE transport, $F_{\text{net},\lambda}$ and $F_{\text{net},\phi}$, while Eq. (8) partitions the divergent circulation into zonal and meridional components, yielding the corresponding vertical velocities ω_λ and ω_ϕ. Substituting these decompositions into Eq. (4) gives separate MSE budgets for the zonal and meridional components:

$$\langle u\, \partial_\lambda (c_p T + L_v q) \rangle + \langle \omega_\lambda\, \partial_p h \rangle + R_\lambda = F_{\text{net},\lambda} \tag{9a}$$

$$\langle v\, \partial_\phi (c_p T + L_v q) \rangle + \langle \omega_\phi\, \partial_p h \rangle + R_\phi = F_{\text{net},\phi}. \tag{9b}$$

Here, the zonal and meridional components sum to the full MSE budget, such that $R = R_\lambda + R_\phi$ and $F_{\mathrm{net}} = F_{\mathrm{net},\lambda} + F_{\mathrm{net},\phi}$. This decomposition allows the energetic constraints on the WC and HC to be diagnosed separately. As only time-mean quantities are considered hereafter, overbars are omitted for clarity. In the tropical atmosphere, horizontal temperature and moisture gradients are weak (Sobel et al. 2001), and transient eddy contributions are small. Hence, we approximate the leading-order balance as that between vertical MSE advection and the net energetic input:

$$\delta\langle \omega_x\, \partial_p h\rangle \approx \delta F_{\mathrm{net},x} \qquad (10)$$

where the subscript *x* represents either the zonal component (λ), associated with the Walker circulation, or the meridional (ϕ) component, associated with the Hadley circulation. This approximation implies that changes in the net energy input are accommodated primarily through changes in vertical MSE advection. The validity of Eq. (10) is assessed quantitatively in Section 4.1.

b. Gross moist stability and circulation strength

To relate the overturning circulation strength to the atmospheric energy budget, we adopt a gross moist stability framework (e.g., Wills et al. 2017). For each component, λ and ϕ (collectively denoted by *x*), the gross moist stability GMS is defined as

$$GMS_x \equiv -g\,\frac{\langle \omega_x \partial_p h\rangle}{\omega_{500,x}}, \qquad (11)$$

where g is the gravitational acceleration, $\langle \omega \partial_p h\rangle$ is the vertically integrated vertical MSE advection, and ω_{500} is the mid-tropospheric vertical velocity at 500 hPa. Physically, gross moist stability measures the energetic stratification experienced by the overturning circulation, that is, the amount of MSE export per unit circulation strength.

This formulation allows changes in circulation strength $\omega_{500,x}$ to be attributed to changes in either vertical MSE advection or GMS:

$$\frac{\delta\omega_{500,x}}{\omega_{500,x}} = \frac{\delta\langle \omega_x\, \partial_p h\rangle}{\langle \omega_x\, \partial_p h\rangle} - \frac{\delta GMS_x}{GMS_x}. \qquad (12)$$

where the δ notation denotes anomalies relative to the control run ($Q_1 = 0$). Eq. (12) is useful because $\omega_{500,x}$, which is a measure of overturning strength of either the Walker circulation (Kosovelj and Zaplotnik 2023) or the Hadley circulation (Picovnik et al. 2022), is directly linked to the atmospheric energy budget (e.g. Eq. (9)) through the vertical advection term.

We next assume that GMS remains approximately constant in response to zonally antisymmetric perturbation Q_{WC}, because the perturbation has zero tropical mean and therefore does not directly alter the tropical-mean energetic state. Indeed, the tropopause height, a first-order proxy for changes in GMS (Wills et al. 2017, Fan and Dommenget 2021), remains nearly unchanged in our simulations (Fig. S2). This simplifies Eq. (12) to the following scaling relationships:

$$\delta\omega_{500,\lambda} \approx -g\frac{\delta\langle\omega_\lambda\,\partial_p h\rangle}{GMS_{0,\lambda}} \tag{13a}$$

$$\delta\omega_{500,\phi} \approx -g\frac{\delta\langle\omega_\phi\,\partial_p h\rangle}{GMS_{0,\phi}} \tag{13b}$$

The validity of the constant-GMS approximation adopted in Eq. (13) is assessed quantitatively in Section 4.1.

Combining Eqs. (10) and (13), the changes in the zonal and meridional overturning strengths can be expressed as:

$$\delta\omega_{500,\lambda} \approx -g\frac{\delta F_{\mathrm{net},\lambda}}{GMS_{0,\lambda}} = -g\frac{\delta Q_\lambda\ +\ \delta F_{\mathrm{cld},\lambda} + \delta F_{\mathrm{clr},\lambda}}{GMS_{0,\lambda}} \tag{14a}$$

$$\delta\omega_{500,\phi} \approx -g\frac{\delta F_{\mathrm{net},\phi}}{GMS_{0,\phi}} = -g\frac{\delta Q_\phi\ + \delta F_{\mathrm{cld},\phi} + \delta F_{\mathrm{clr},\phi}}{GMS_{0,\phi}}. \tag{14b}$$

Then, the strengths of the WC and the HC, respectively, are defined as

$$\left[\delta\omega_{500,\lambda}\right]_{wp} \approx -g\frac{[\delta Q_\lambda]_{wp}\ +\ \left[\delta F_{\mathrm{cld},\lambda}\right]_{wp} + \left[\delta F_{\mathrm{clr},\lambda}\right]_{wp}}{\left[GMS_{0,\lambda}\right]_{wp}} \tag{15a}$$

$$\left[\delta\omega_{500,\phi}\right]_{eq} \approx -g\frac{\left[\delta Q_{\phi}\right]_{eq} + \left[\delta F_{\mathrm{cld},\phi}\right]_{eq} + \left[\delta F_{\mathrm{clr},\phi}\right]_{eq}}{\left[GMS_{0,\phi}\right]_{eq}}, \tag{15b}$$

where $[\ ]_{wp}$ denotes an average over the warm patch and $[\ ]_{eq}$ denotes an average over the equatorial band $\phi \leq \pm 5°$.

Finally, in the absence of radiative feedbacks, the circulation responses reduce to

$$\left[\delta\omega_{500,\lambda}\right]_{wp} \approx -g\frac{\left[\delta Q_{\lambda}\right]_{wp}}{\left[GMS_{0,\lambda}\right]_{wp}} \tag{16a}$$

$$\left[\delta\omega_{500,\phi}\right]_{eq} \approx 0 \tag{16b}$$

because $\left[\delta Q_{\phi}\right]_{eq} = 0$ by construction, as the prescribed zonally antisymmetric heat flux has no zonal-mean component. Hence, the no-feedback assumption predicts that increasing Q_{WC} directly strengthens the WC but does not affect the HC strength.

4. Results

a. Walker and Hadley circulation responses to zonally antisymmetric flux Q_{WC}

As intended by the experimental design, the Walker circulation strength scales linearly with the amplitude of Q_{WC} (solid black in Fig. 3a). The changes in simulated WC strength are well approximated by the change in vertical MSE advection given by Eq. (13a) (blue solid line), indicating that contributions from GMS changes are negligible. Moreover, the approximation that F_{net} anomalies are balanced by vertical advection anomalies, as in Eq. (10), also aligns closely with the simulated response, with a slight overestimation of the amplitude (red solid line). This agreement suggests that horizontal advection and eddy contributions are small. Finally, the no-radiative-feedback approximation (Eq. (16a); dashed black line) captures the WC response well, indicating that radiative feedbacks do not strongly modulate WC strength. Thus, in our experiment configurations, changes in the prescribed zonally antisymmetric surface heat flux can be interpreted as direct changes in WC strength.

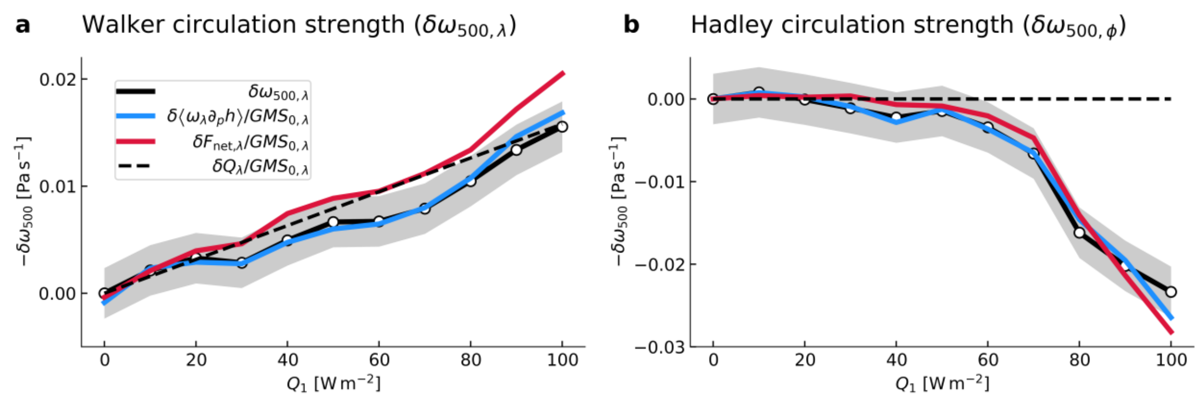

Fig. 3. Circulation strength anomaly, measured by $\delta\omega_{500,x}$ (black) as well as successive approximations assuming constant *GMS* (Eq. 13; blue), neglecting horizontal MSE advection and transient eddies in addition to the constant-*GMS* assumption (Eq. 15; red), and further neglecting radiative feedbacks (Eq. 16; black dashed), for (a) the Walker circulation and (b) the Hadley circulation. Shading indicates the 95% confidence interval estimated from monthly variability in the control run.

Figure 3b shows how the Hadley circulation strength responds to changes in Walker circulation strength. Because the zonal mean component of the prescribed Q_{WC} is zero, one would not expect a directly forced change in the zonal-mean Hadley circulation strength under no-feedback approximation (Eq. (16b); dashed black line). For weak to moderate forcing amplitudes ($0 < Q_1 < 60$ W m^{-2}), the Hadley circulation strength remains largely unchanged, consistent with the fact that the imposed Q_{WC} does not alter the zonal-mean net energy input. However, the simulated response (black solid) deviates markedly from this expectation for $Q_1 > 70$ W m^{-2}, where the HC exhibits a pronounced weakening. In the strongest forcing case, $Q_1 = 100$ W m^{-2}, the HC weakens by more than 0.02 Pa s^{-1}, corresponding to a 46% decrease relative to the control state. The transition between these two regimes suggests the existence of a threshold WC strength beyond which the HC becomes sensitive to the imposed zonal asymmetry. As in the case for the WC scaling, the HC response is well captured by changes in vertical MSE advection (Eq. (13b); blue line), indicating that *GMS* changes are negligible. Similarly, the approximation of HC strength based on changes in F_{net} (Eq. (15b); red line) closely follows the simulated HC response, suggesting that contributions from horizontal advection and eddies remain small. In contrast, the HC strength deviates substantially from the no-feedback assumption (Eq. (16b); dashed black), indicating that radiative feedbacks are responsible for the strong sensitivity of HC strength at large Q_1. We therefore proceed to investigate how radiative feedbacks respond across the different forcing regimes.

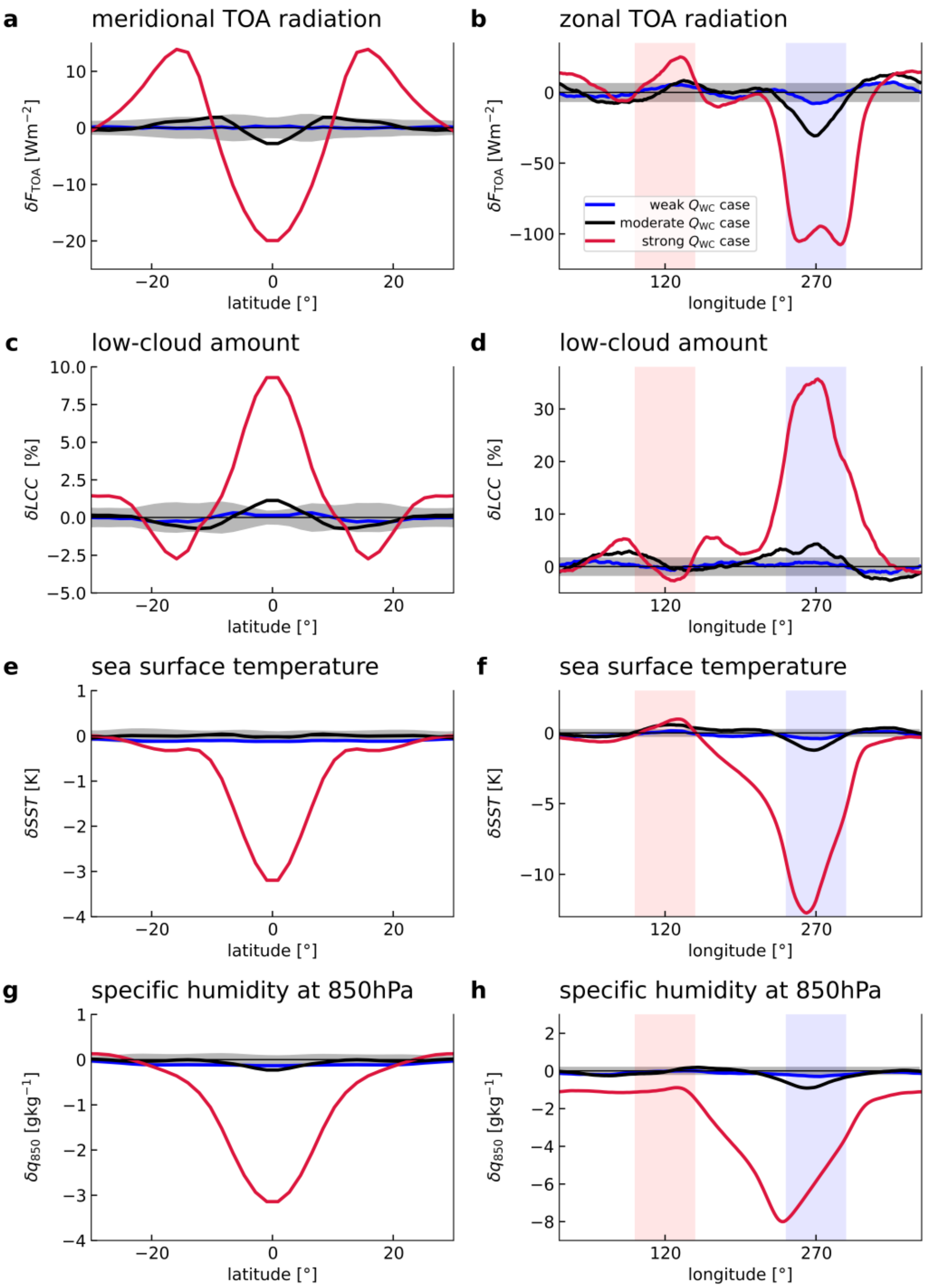

Fig. 4. Anomalies in (a,b) F_{TOA}, (c,d) low cloud cover, (e,f) SST and (g,h) specific humidity for the weak (blue), moderate (black), and strong (red) Q_{WC} cases. The left column shows zonal-mean latitudinal profiles, and the right column shows equatorial-mean longitudinal profiles averaged over $\varphi \leq \pm 5°$. Red and blue vertical shading indicate the extent of the warm and cold patches, respectively. Gray shading indicates the 95% confidence interval based on monthly variability in the control run.

b. The role of cloud radiative effects

We focus on three representative Q_{WC} forcing amplitudes: a weak case ($Q_1 = 20\ \mathrm{W\,m^{-2}}$), a moderate case ($Q_1 = 60\ \mathrm{W\,m^{-2}}$), and a strong case ($Q_1 = 100\ \mathrm{W\,m^{-2}}$), corresponding, respectively, to the HC-insensitive regime, the threshold regime, and the anti-correlated regime, identified in Fig. 3b.

In the weak forcing case (blue line in Fig. 4), Q_{WC} produces no significant change in the zonal-mean F_{TOA} (Fig. 4a). Along the equator, the F_{TOA} anomalies over the warm and cold patches are nearly symmetric, resulting in negligible zonal-mean response (Fig. 4b). According to Eq. (16b), which relates HC strength to the zonal-mean F_{TOA} anomaly, the near-zero zonal-mean F_{TOA} anomaly implies that the HC strength remains largely unaffected.

In the moderate forcing case (black line in Fig. 4), a marginally significant decrease in zonal-mean F_{TOA} emerges in the equatorial region (Fig. 4a). This reduction is primarily driven by the response over the cold patch (Fig. 4b), where modest but significant local SST cooling (Fig. 4h) slightly enhances low-cloud cover (Fig. 4d), thereby reducing F_{TOA}. According to Eq. (16b), the resulting small reduction in equatorial zonal-mean F_{TOA} implies a slight weakening of the HC, consistent with Fig. 3b.

In the strong forcing case (red line in Fig. 4), the zonal-mean F_{TOA} decreases strongly in the equatorial region (Fig. 4a). This decrease consists of a 60% contribution from the cloud-radiative response δF_{cld} (Fig. 5a) and a 40% contribution from the clear-sky response δF_{clr} (Fig. 5c). The radiative cooling associated with δF_{cld} results from enhanced low cloud cover over the cold patch (Fig. 4d), induced by pronounced local SST cooling (Fig. 4f). This points to a positive low-cloud feedback mechanism: local SST cooling stabilizes the lower troposphere and promotes low-cloud formation, which in turn further amplifies the local SST anomaly (Wood and Bretherton 2006). Consistently, the Q_{WC}-driven SST cooling over the cold patch is mainly amplified by reduced shortwave radiation (Fig. S3). This shortwave-induced SST cooling is confined to the cold patch (Fig. S3), consistent with the localized low-cloud response (Fig. 4d), but substantial SST cooling extends westward of the cold patch (Fig. 4f). This westward extension of cooling is primarily attributable to enhanced latent heat flux associated with intensified easterlies (Fig. S3). Following this cooling, substantial atmospheric drying occurs over the cold patch and farther westward (Fig. 5h), leading to enhanced clear-sky outgoing longwave radiation (i.e., negative δF_{clr}) across this broad region (Fig. 5d). Together, δF_{clr} and δF_{cld} contribute a pronounced decrease in equatorial F_{TOA}, consistent with the strong weakening of the HC shown in Fig. 3b for the strong Q_{WC} case.

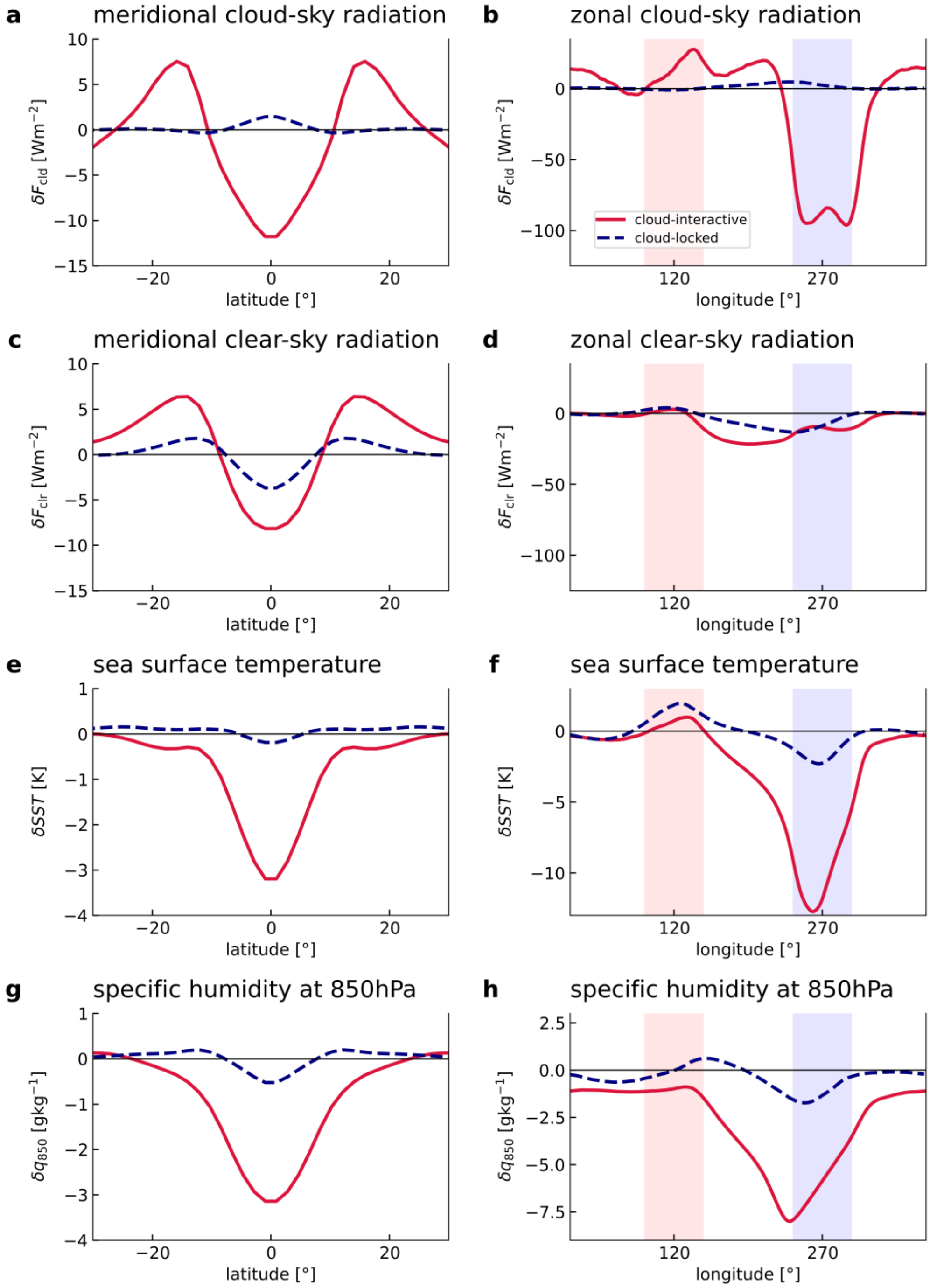

Fig. 5. Comparison of anomalous (a,b) clear-sky radiation δF_{clr}, (c,d) cloud-sky radiation δF_{cld}, (e,f) sea surface temperature δSST, and (g,h) 850 hPa specific humidity δq_{850} for the strong Q_{WC} case with locked clouds (blue) and interactive clouds (red). Zonal mean latitudinal profile on the left and equatorial mean $\varphi \leq \pm 5°$ longitudinal profile on the right. Red and blue vertical shading indicate the extent of the warm and cold patches, respectively.

Examination of the different forcing amplitude cases indicates that the HC undergoes a regime transition when the cold-patch cooling becomes sufficiently strong to activate a positive low-cloud feedback. The moderate forcing scenario marks the onset of this feedback, and thus the beginning of the regime transition. These results point to the central role for cloud radiative feedbacks in shaping the HC response across forcing regimes. To verify this, we conduct cloud-locked runs in which cloud radiative feedbacks are suppressed (Kang et al. 2008; Voigt and Shaw 2015). In the locked simulations, as intended, the cloud-radiative response δF_{cld} is largely muted (Fig. 5a,b). As cloud radiative feedbacks are absent, the cooling over the cold patch is substantially damped (Fig. 5f), which in turn weakens the atmospheric drying response (Fig. 5h). Consequently, the clear-sky radiative response δF_{clr} is also substantially reduced (Fig. 5c,d), indicating that the clear-sky response arises indirectly from cloud radiative feedbacks. As a result of the damped net δF_{TOA}, the HC weakening is strongly reduced for large Q_1, such that the HC response exhibits little sensitivity to the WC response in cloud-locked simulations (Fig. 6b). This confirms that cloud radiative feedbacks mediate the shift from an HC regime insensitive to WC changes to one in which the two circulations are anti-correlated.

However, a weak HC sensitivity persists in the cloud-locked run, exceeding internal variability under strong forcing (blue in Fig. 6b). This is because the constant-GMS approximation no longer holds. In the cloud-interactive case under strong Q_{WC} forcing, the HC weakening ($\delta\omega_{500,\phi}/\omega_{500,\phi} = -46\%$) can be attributed primarily to weakened vertical advection ($\delta\langle\omega_\phi\,\partial_p h\rangle/\langle\omega_\phi\,\partial_p h\rangle = -52\%$), which is only partly offset by reduced GMS ($\delta GMS/GMS = -6\%$). Thus, the vertical advection term outweighs the GMS response by an order of magnitude, supporting the validity of the constant-GMS approximation in the cloud-interactive case (Eqs. (13) and (14); Fig. 3b). In contrast, for the cloud-locked case, the HC weakening ($\delta\omega_{500,\phi}/\omega_{500,\phi} = -12\%$) largely results from enhanced GMS ($\delta GMS/GMS = +9\%$), with a smaller contribution from weakened vertical advection. Hence, the HC weakening in the cloud-locked case in Fig. 6b is associated with enhanced GMS.

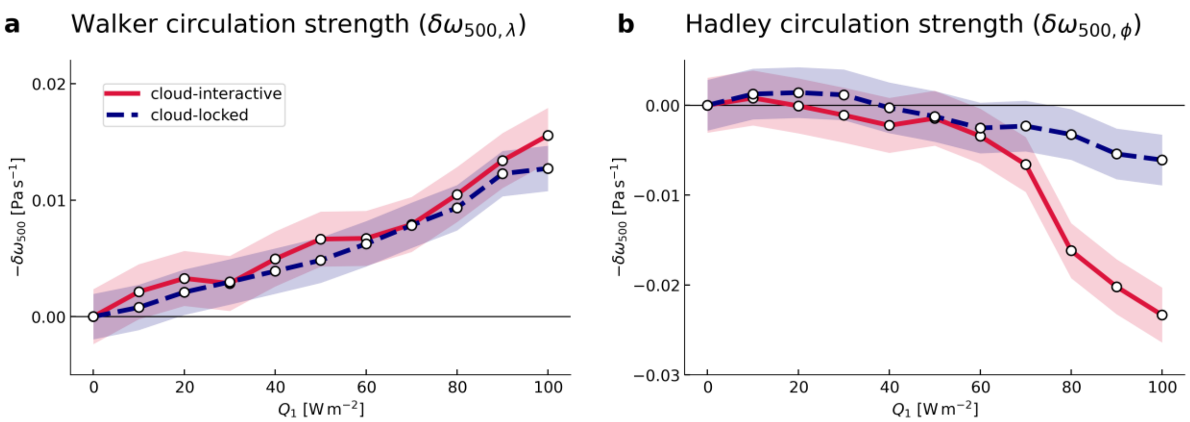

Fig. 6. Circulation strength anomalies of the (a) Walker circulation $\delta\omega_{500,\lambda}$ and (b) Hadley circulation $\delta\omega_{500,\phi}$ in the cloud-interactive (red solid) and cloud-locked (blue dashed) runs. Shading indicates the 95% confidence interval based on monthly variability in the control run.

The cloud-locking experiments clearly highlight the importance of low-cloud feedback in mediating the anti-correlated response between Walker and Hadley circulation strengths. This naturally raises the question of what drives the low-cloud feedback.

c. Relative impacts of the warm and cold patches

The radiatively locked cloud simulations clearly show that the coupling between WC and HC is mediated by low-cloud feedback over the cold patch. However, it remains unclear to what extent the enhanced low-cloud formation reflects a purely local response to the cold patch, as opposed to a remote effect originating from the warm patch. On the one hand, a local mechanism may operate: the prescribed cooling over the cold patch reduces local SSTs, and strengthens the lower-tropospheric stability and the temperature inversion, thereby promoting low-cloud formation (Wood and Bretherton 2006). This locally enhanced cloudiness can then be further amplified by positive low-cloud radiative feedback. On the other hand, a remote, nonlocal mechanism may also contribute. Enhanced deep convection over the warm patch induces upper tropospheric warming across the tropics via gravity waves (Bretherton and Smolarkiewicz 1989). This large-scale tropospheric adjustment alters the vertical temperature structure over distant regions (Zhang and Fueglistaler 2020), including the cold patch. The resulting upper-level warming increases lower-tropospheric static stability over the cold patch, favoring low-cloud formation (Andrews and Webb 2018). That is, low-cloud enhancement over the cold patch can be mediated by large-scale dynamical adjustment to remote heating over the warm patch (Zhou et al. 2016). Such remotely induced stabilization may then be further amplified by low-cloud radiative feedback, reinforcing the zonal asymmetry in TOA radiation.

To address this question, we conduct a set of single-patch forcing experiments for the strong Q_{WC} forcing case, designed to isolate the effects of remote warming and local cooling. The results show that the SST response exhibits strong nonlinearity to cooling and heating of equal amplitude. The prescribed heating of $Q_1 = 100\ \mathrm{W\,m^{-2}}$ produces only a modest SST increase, with maximum warming of 2.2 K at the center of the warm patch (Fig. 7a). This is consistent with negative feedbacks that constrain the upper bound of tropical SSTs to around 29-30°C via enhanced evaporative cooling (Hartmann and Michelsen 1993, Sud et al. 1999), local cloud albedo feedback (Ramathan and Collins 1991), and heat transport feedback (Sun and Trenberth 1998). In contrast, cooling of the same magnitude leads to a pronounced SST decrease of up to 17.5 K at the center of the cold patch, with the cooling pattern extending westward from the forcing region (Fig. 7b).

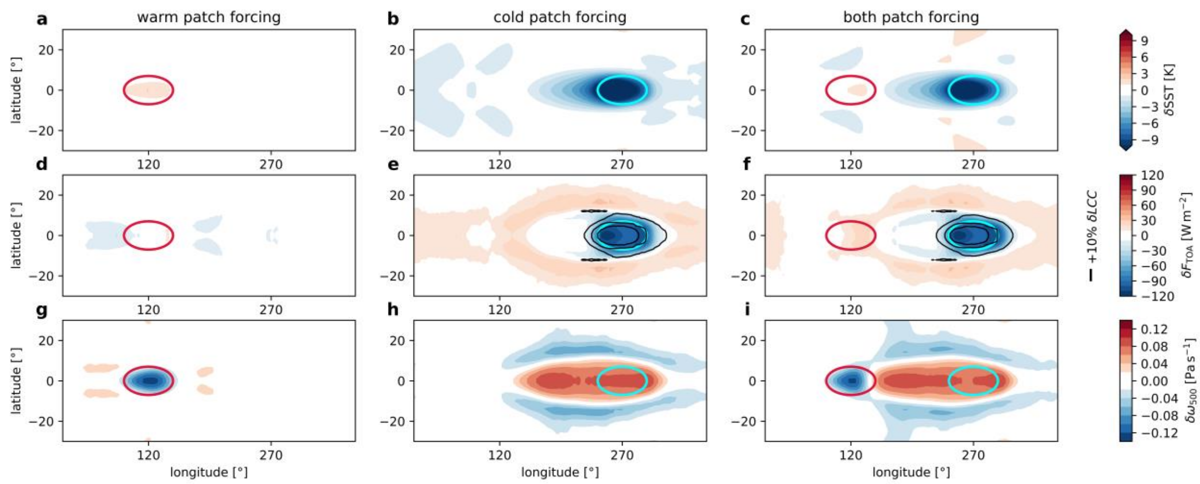

Fig. 7. Anomalies in (a-c) SST, (d-f) F_{TOA}, and (g-i) ω_{500} for the strong Q_{WC} case ($Q_1 = 100\ \mathrm{W\,m^{-2}}$) in the (a,d,g) warm-patch forcing, (b,e,h) cold-patch forcing, and (c,f,i) default configuration with both patches. Black contours in panels (d-f) show low cloud cover increase at 10% intervals. Red and cyan ovals mark the warm- and cold-patch regions, respectively.

Consistent with this stark asymmetry in SST anomaly, the radiative response is governed primarily by the cold patch (Fig. 7d-f). Localized heating over the warm patch produces negligible remote radiative effects, with outgoing longwave radiation increasing only weakly (Fig. 7d). In contrast, the F_{TOA} response to cooling over the cold patch is substantially stronger, both in spatial extent and magnitude (Fig. 7e). The strongly negative F_{TOA} response around the cold patch is due to enhanced low-cloud cover (black solid in Fig. 7e). Notably, the westward extension of cold SST anomalies seen in Fig. 7b is not reflected in the F_{TOA} response because of the compensating effects between the cloud radiative effects and clear-sky radiative responses (Fig. 5b,d). The westward extended SST cooling is instead due to enhanced latent heat fluxes associated with strengthened easterlies (Fig. S3).

Similarly, large-scale vertical motion exhibits a strong asymmetry in its response to the warm and cold patches. The overall reorganization of convection is driven primarily by the cold patch rather than the warm patch (Fig. 7g-i). While the warm patch induces enhanced deep convection locally, the cold patch produces a more widespread dynamical response, characterized by pronounced subsidence over and far west of the cold patch, accompanied by compensating ascent in the surrounding region. The extent of the subsiding region is consistent with the SST response (Fig. 7b,h). The compensating ascent organizes predominantly in the meridional direction rather than zonally (Fig. 7h). Such a pronounced meridional redistribution of vertical motion, marked by anomalous equatorial subsidence and off-equatorial ascent, implies a HC weakening, consistent with Fig. 3b. This raises the question of whether there is an a priori dynamical constraint that requires this reorganization to preferentially occur in the meridional direction. We address this question in the next section.

The single patch experiments indicate that the low cloud feedback over the cold patch, identified as responsible for the anticorrelated HC-WC coupling (Section 4.3), is driven by local cooling rather than remote warming from the warm patch. Thus, the low cloud formation over the cold patch is controlled primarily by local inversion strengthening induced by surface cooling, rather than by remotely induced free-tropospheric warming associated with the warm-patch heating. Consistently, the off-equatorial anomalous ascent, indicative of HC weakening, is almost entirely reproduced by cooling the cold patch alone (Fig. 7h,i).

d. How convective instability links the Walker and Hadley circulations

In this section, we introduce a conceptual framework that provides an intuitive interpretation of the results presented above. A cornerstone of tropical atmospheric dynamics is the concept of convective quasi-equilibrium (Betts 1982, Emanuel 2007, Raymond 1995), which posits that deep convection relaxes the free-tropospheric temperature profile toward a moist adiabat set by the thermodynamic properties of the subcloud layer. Because a moist adiabat corresponds approximately to constant saturation MSE, this implies that, in convective regions, the saturation MSE of the free troposphere closely matches the subcloud MSE. That is, deep convection exports subcloud MSE upward and thereby regulates the thermodynamic state of the tropical free troposphere. A key implication is that convection in one region can influence the broader tropical atmosphere. By setting the saturation MSE aloft, deep convective regions effectively establish a background threshold for convection elsewhere (Zhang and Fueglistaler 2020). Where subcloud MSE exceeds the ambient free-tropospheric saturation MSE, deep convection can be sustained; where it does not, convection is suppressed and subsidence prevails. To quantify this behaviour, we define a convective instability index as the difference between subcloud MSE and saturation MSE at 500 hPa, taken here as representative of the free troposphere, following Williams and Pierrehumbert (2017): $h_0 - h_{500}^*$. Positive values indicate conditions favorable for deep convection, whereas negative values correspond to convectively stable, subsiding regions.

This framework can be visualized using the circus tent analogy (Williams et al. 2023). In this picture, subcloud MSE h_0 represents the tent poles and free-tropospheric saturation MSE h_{500}^* forms the tent fabric. Gravity waves efficiently homogenize MSE anomalies in the free troposphere, maintaining the large-scale coherence of the fabric across the tropics. Deep convection occurs where the poles rise high enough to contact and lift the fabric, that is, where subcloud MSE exceeds the ambient free-tropospheric threshold, while regions where the poles fall short remain in subsidence.

In our control setup under zonally symmetric aquaplanet conditions, deep convection is permitted across the equator: in the tent-pole analogy, the pole touches the fabric, and the convective instability index is near zero or positive there (Fig. 8a, red dashed line). Prior studies have emphasized that tropical free-tropospheric adjustment to changes in deep convection plays a crucial role in stabilizing or destabilizing remote regions (Zhou et al. 2016, Andrews and Webb 2018, Dong et al. 2019). This perspective can be interpreted through the tent-pole analogy as follows. The warm patch would be expected to raise the "tent pole", corresponding to a local h_0 increase, and thereby lift the free-tropospheric "fabric", increasing h_{500}^* across the tropics. Remote regions would then become detached from the fabric: convection would be inhibited and subsidence would prevail, effectively shrinking the convective area (Bretherton and Sobel 2002). This suggests that the warm patch should exert a broad stabilizing impact. However, this interpretation assumes that the remote subcloud MSE h_0 remains fixed, an assumption that is valid for fixed SST configurations. In a coupled system, h_0 also adjusts in remote regions. Indeed, in our warm patch experiment, changes in h_{500}^* and h_0 are of comparable magnitude, so the convective instability index changes only weakly (Fig. 8d). This contrasts with fixed-SST setups (illustrated in Fig. 8a), in which remote regions are stabilized by increases in free tropospheric saturation MSE h^*_{500} while their subcloud MSE h_0 remains unaffected. However, in the coupled slab-ocean setup, where SSTs are allowed to adjust to perturbations, the compensating responses of h^*_{500} and h_0 strongly mask this non-local stability mechanism (Fig. 8d).

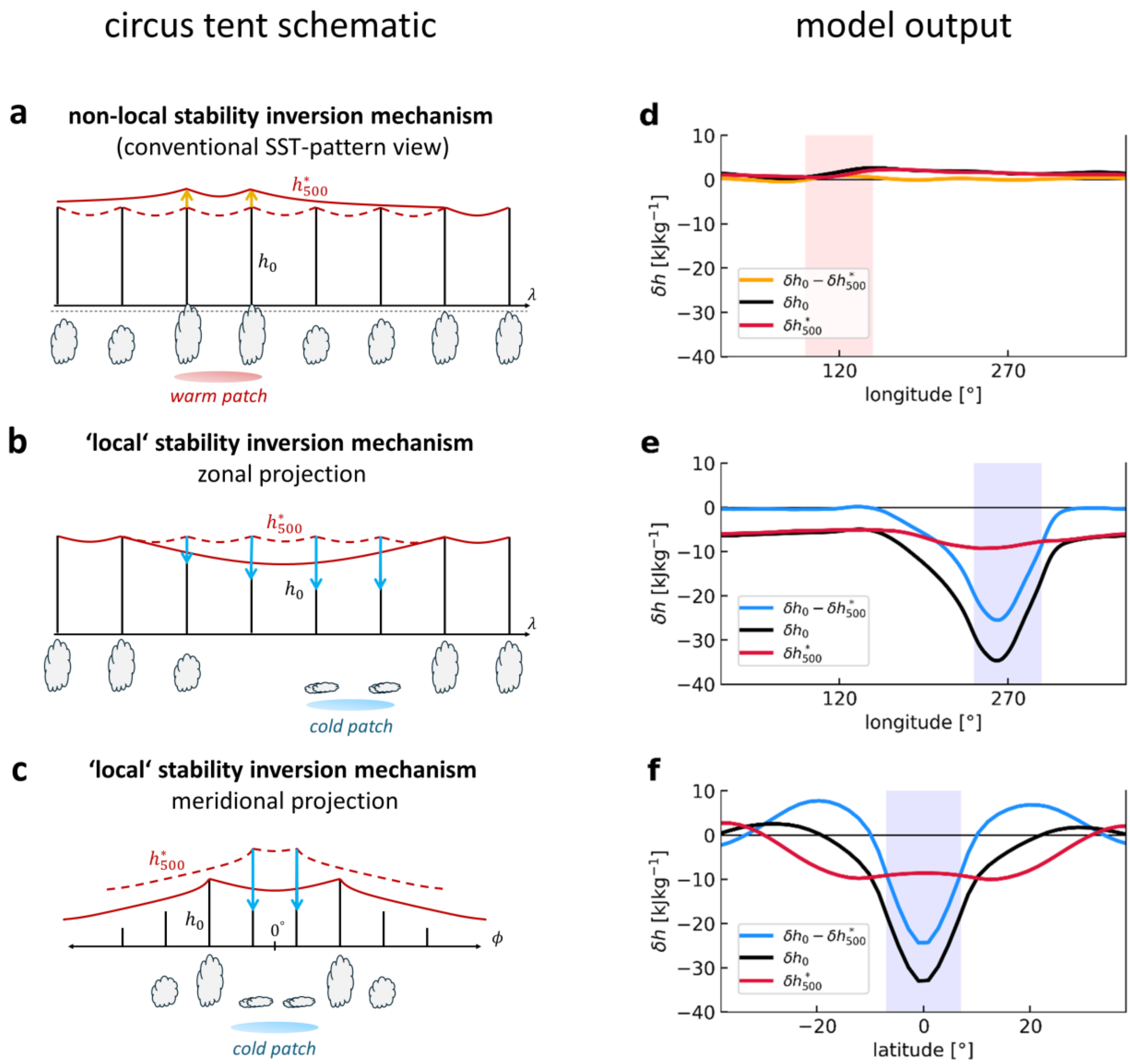

Fig. 8. Changes in circus tent pole height (black) and fabric height (red) induced by (a) warming or (b,c) cooling a localized equatorial patch through a prescribed energetic perturbation. Panels (a) and (b) show zonal projections of the three-dimensional tent structure, whereas panel (c) shows a meridional projection through the cold patch. Panels (d-f) show the corresponding model-simulated anomalies in subcloud MSE h_0 (black), free-troposphere saturation MSE h^*_{500} (red), and the convective instability index $h_0 - h^*_{500}$ (blue).

We next examine the response to a cold patch in the conventional fixed-SST framework. Cooling in subsiding regions is assumed to have only a limited, local effect: a cold patch would reduce the local subcloud MSE h_0, while leaving the free tropospheric saturated MSE h^*_{500}

largely unchanged, so that deep convection would be inhibited only locally over the cooled region. However, our cold patch experiment exhibits a spatially extensive SST response that is much larger than in the warm patch experiment (Fig. 7a,b). The westward-extended SST cooling is strong enough to dry the entire equatorial band (Fig. 5h), leading to a broad reduction in h_0, with the largest reductions over and west of the cold patch. The free troposphere saturation MSE h^*_{500} then decreases nearly uniformly across the equatorial region, following the reduction in h_0 over the relatively warm convective regions outside the cold patch (Fig. 8e). In the circus tent analogy, this corresponds to the tent poles shrinking over a broad region and effectively detaching from the now loose tent fabric (Fig. 8b). Thus, convection is stabilized over a broad region by localized cooling, not aligned with the conventional picture of a local stability-inversion mechanism. The convective instability anomalies exhibit a striking asymmetry between the warm-patch and cold-patch experiments (Fig. 8d,e), consistent with the asymmetry in the SST response (Fig. 7a-c). It is this nonlinear nature of SST response to surface heat flux forcing that makes the warm patch much less effective than the cold patch at inducing MSE changes.

Let us now examine the meridional structure of convection. In the control setup, deep convection occurs along the equatorial band, with subsidence in the subtropics (red dashed in Fig. 8c). When the cold patch is prescribed, the equatorial band cools substantially (Fig. 7b), which in the tent analogy corresponds to the equatorial tent poles detaching from the tent fabric. As the fabric loosens, it begins to rest on the next-highest tent poles. Because the equatorial cooling is so strong, these poles are no longer located within the original equatorial ascending region, but instead in the adjacent off-equatorial regions that were formerly subsiding (solid red in Fig. 8c). In terms of the convective instability index (Fig. 8f), this corresponds to a narrow latitudinal corridor, comparable in scale to the cold patch (blue shading), where changes in h_0 (black line) dominate over changes in h^*_{500} (red). As a result, $h_0 - h^*_{500}$ (blue) becomes anomalously negative, indicating suppressed deep convection. In adjacent regions outside this equatorial band, however, changes in h^*_{500} dominate over changes in h_0, making the atmosphere unstable to deep convection. In other words, the reduction in the convective threshold through lower h^*_{500} allows off-equatorial regions to participate in deep convection. This is in good agreement with the meridional reorganization of convection shown in Fig. 7i.

While the original tent analogy was proposed to describe zonal convective reorganization (Williams et al. 2023), our slab ocean results suggest that it can also be extended to explain the meridional reorganization. In the present setup, the SST response induced by the localized cold-patch cooling extends over more than 100° in longitude but only about 10° in latitude. Its broad zonal extent produces a widespread reduction in free-tropospheric MSE (red in Fig. 8f), thereby lowering the subcloud MSE required for deep convection, whereas its narrow meridional width confines the reduction in subcloud MSE to the equatorial region (black in Fig. 8f). Consequently, the meridionally adjacent regions experience a lowered convective threshold, making them preferred locations for convective reorganization. In contrast, the warm patch exerts only a weak influence (Fig. 8d) because its SST response is too small to produce comparable changes in free-tropospheric thermodynamic state. We therefore identify the cold patch region as the key driver of structural changes in meridional convective organization, owing to the large SST response amplified by low cloud feedbacks. The resulting large-scale cooling reduces free-tropospheric saturation MSE over adjacent latitudes through gravity-wave adjustment. This interaction between the cold patch and the neighboring latitudes intrinsically links WC changes to HC changes: cold-patch dynamics translates a strengthening or weakening of the WC into a meridional reorganization of convection, which in turn weakens or strengthens the HC, respectively. The resulting WC-HC relationship is therefore inherently anti-correlated.

e. Limitations of the energetic framework

The energetic framework serves as a central pillar of this study, allowing us to relate changes in the WC and HC to changes in TOA radiative fluxes (Eq. (15)). Through this relationship, we identify cloud radiative feedbacks as the key mediator of WC-HC coupling (Section 4.2). The same energetic framework has also been used to infer the two-dimensional structure of meridional shifts in convective regions through the energy flux potential (Boos and Korty 2016). In principle, it should therefore also capture the meridional reorganization of convection found in our simulations (Fig. 7i). However, as shown below, the energetic framework does not fully capture the spatial pattern of the response in the present configuration.

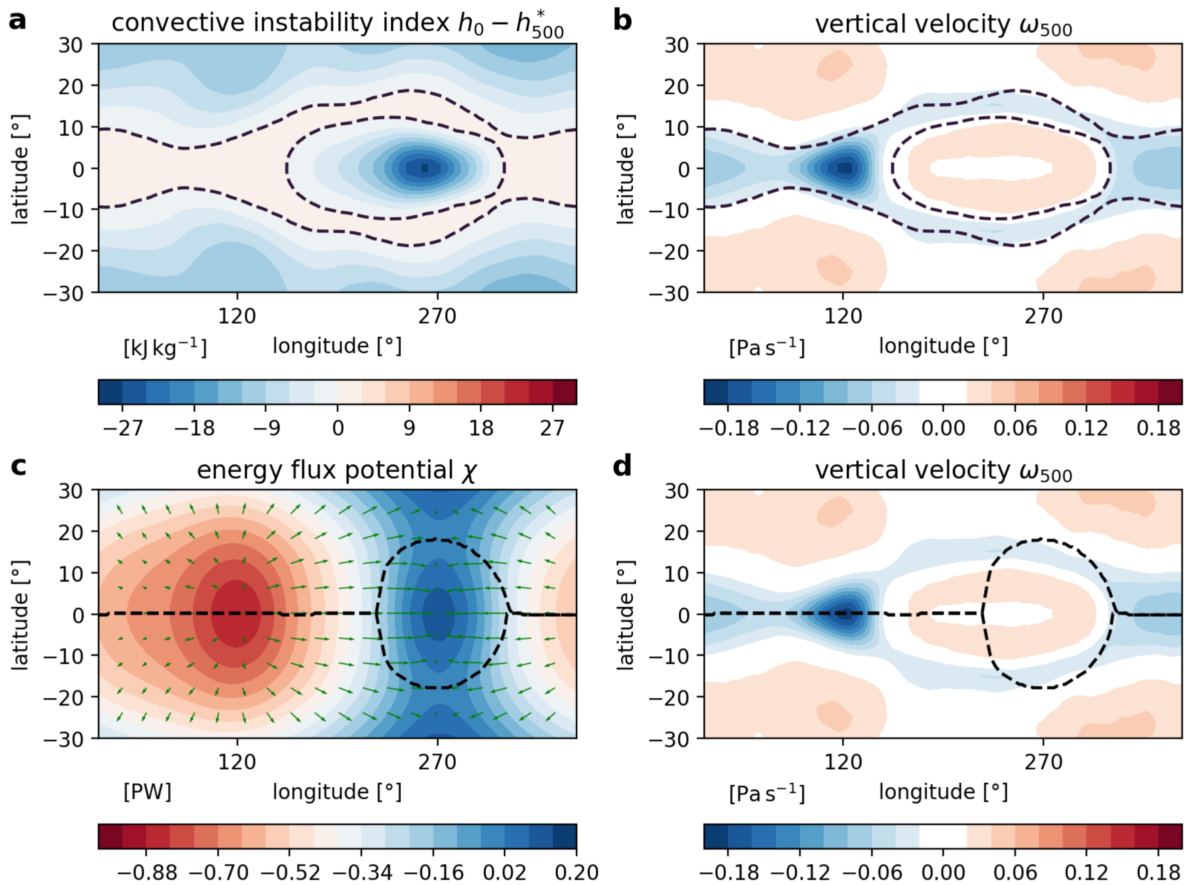

Fig. 9. Comparison of convective-region boundaries diagnosed from the convective-instability and energetic frameworks under strong forcing. Shading shows (a) the convective instability index and (b) 500-hPa pressure vertical velocity, with the zero crossing of the convective instability index indicated by the dashed line in both panels. Shading shows (c) the energy flux potential and (d) 500-hPa pressure vertical velocity, with the energetic flux equator, defined as the zero crossing of the meridional MSE transport, indicated by the dashed line in both panels.

Our results highlight that SST anomalies can strongly influence the thermodynamic environment for convection by modifying subcloud MSE (Fig. 8e), yet this influence is not well reflected in the TOA radiation response. For example, the westward extension of the cold-patch response is evident in SST (Fig. 7c), subcloud MSE (Fig. 8e), and vertical updraft anomalies (Fig. 7f), whereas the TOA radiation response remains largely confined to the cold patch region (Figs. 4b and 7f). This spatial mismatch limits the prognostic capability of the energetic framework.

This limitation is illustrated by comparing the spatial structures inferred from the two frameworks. While the convective instability index (Fig. 9a) captures the extent and shape of the simulated convective region (Fig. 9b), the energy flux potential (Fig. 9c) performs less well in reproducing the shape of the ascending region (Fig. 9d), particularly where SST and F_{net}

anomalies are not spatially aligned (Fig. 7c,f). The energetic framework captures the imprint of F_{net} on the circulation through the atmospheric energy budget (Eq. (5)), but it does not inherently contain information about the SST anomaly pattern. Because the SST anomaly over the cold patch and its westward extension are crucial for explaining the threshold behaviour that reorganizes tropical convection and subsidence, this reveals an important limitation of the enegetic framework.

f. Comparison with reanalysis data

Our experiment design is highly idealized and is intended to provide qualitative insight into a potential intrinsic link between the WC and HC. This naturally raises the question of whether our results are applicable to real-world conditions. While a full assessment is beyond the scope of this study, we can gain some intuition by comparing the convection pattern in our idealized experiment with the climatology derived from ERA5 reanalysis.

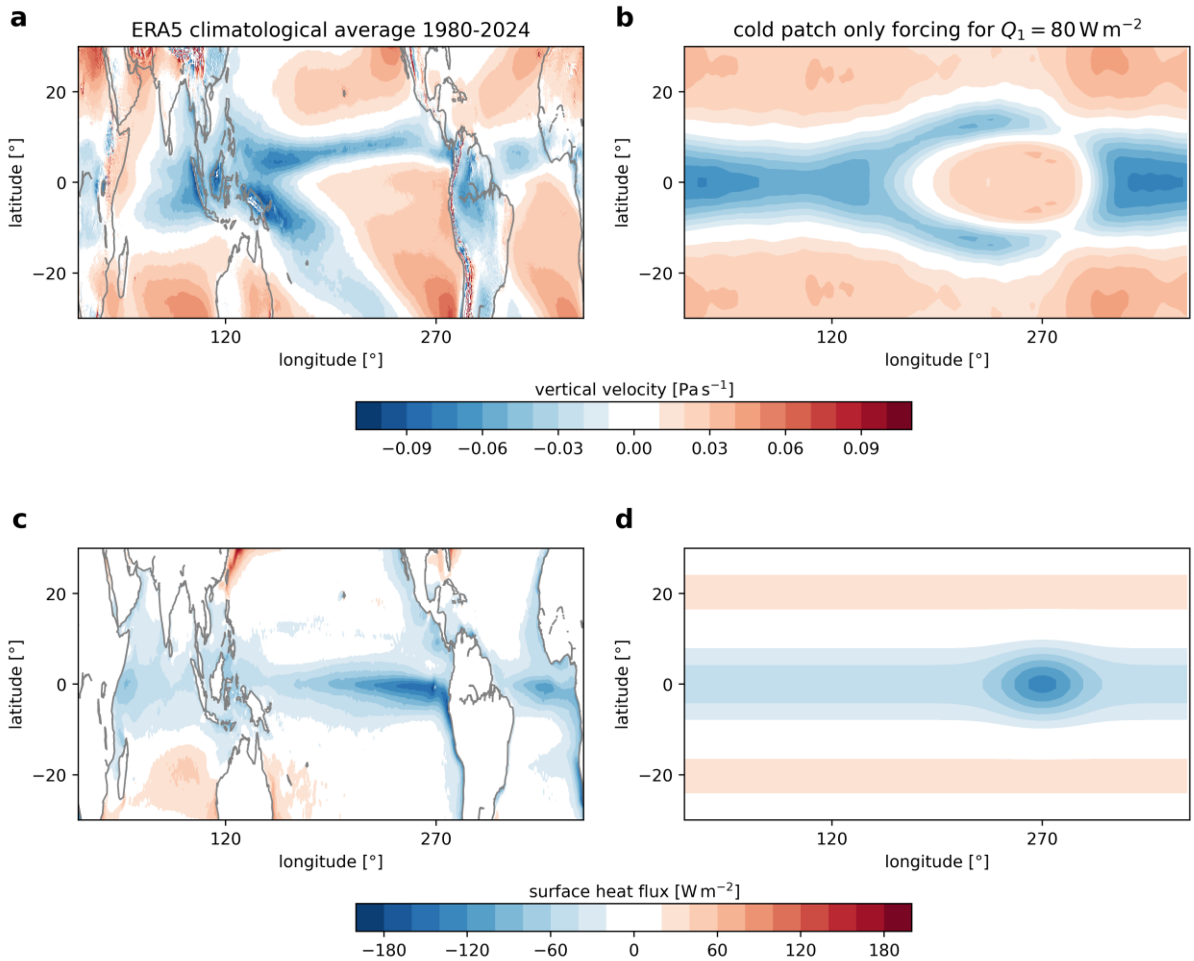

Fig. 10. (a) Pressure vertical velocity at 500 hPa and (c) net surface heat flux for the 1980–2024 ERA5 climatology. (b,d) Similar to (a,c) but for the aquaplanet slab-ocean experiment

forced by a prescribed cold-patch-only heat flux of $Q_1 = 80\ \mathrm{W\ m^{-2}}$. In (a) and (c), blue indicates ascent and red indicates subsidence.

Qualitatively, our experiment shows striking similarities to the ERA5 climatology in the spatial pattern of deep convection. Figure 10a presents the mid-tropospheric vertical velocity from ERA5 reanalysis averaged over 1980–2024, showing a bifurcated structure in which the Pacific Inter-Tropical Convergence Zone is displaced northward and the Southern Pacific Convergence Zone extends southeastward from the western tropical Pacific. We then compare this pattern with that from the cold-patch-only experiment, in which the prescribed surface heat flux (Fig. 10d) broadly resembles the observed surface energy flux pattern (Fig. 10c). Some mismatches are naturally expected given the idealized nature of our experiment setup that omits major components of the Earth system such as the seasonal cycle, land masses, and a dynamical ocean. For example, the precipitation pattern over the southeastern Pacific is known to be strongly influenced by the presence of the Andes (Takahashi and Battisti 2007). Remarkably, despite these simplifications, the cold-patch-only experiment with $Q_1 = 80\ \mathrm{W\ m^{-2}}$ still broadly reproduces the key features of the convective pattern, including both its latitudinal and longitudinal extent (Fig. 10b). This suggests that the eastern Pacific cooling may play a crucial role in shaping the large-scale pattern of deep convection over the tropical Pacific. The relative importance of the western Pacific warm pool and the eastern Pacific cold tongue in setting this pattern warrants further investigation.

5. Summary and Conclusion

This study investigates the intrinsic dynamical link between the Walker circulation (WC) and the Hadley circulation (HC) using an idealized aquaplanet slab ocean model. While the role of ocean dynamics in modulating this relationship is an important question for future work, here we focus on the atmospherically driven processes that couple the two circulations. We prescribe a zonally antisymmetric surface heat flux that mimics the western Pacific warm pool and the eastern Pacific cold tongue, and systematically vary its amplitude to alter the WC strength. As the WC strength increases, the HC response undergoes a regime transition: for weak to moderate WC forcing, the HC remains largely insensitive to changes in WC strength, whereas beyond a critical forcing threshold, the HC weakens substantially, indicating an anticorrelated relationship between WC and HC strength.

Single-patch experiments show that the WC-HC coupling is primarily governed by the cold patch. Warm-patch forcing enhances local convection only marginally, accompanied by weak SST and MSE anomalies, thereby exerting a limited influence on the large-scale circulation. In contrast, cold-patch forcing alone almost entirely reproduces the full response, including the HC weakening. This cold-patch response is mediated by low cloud feedback. When the cold patch becomes sufficiently strong, low clouds form and the associated radiative feedback amplifies the local SST cooling. This cooling strengthens the easterlies west of the cold patch, extending the cooling westward through enhanced evaporation. Increased low cloud cover enhances shortwave reflection, while the resulting cooling and drying increases clear-sky outgoing longwave radiation. Both effects act to reduce net energy input (NEI) into the atmospheric column within the equatorial band. The HC therefore weakens in response to this low-cloud-driven NEI reduction. The key role of cloud radiative feedback in mediating the WC-HC coupling is confirmed by the cloud-locked simulations. Suppressing cloud radiative feedbacks strongly damps the SST and humidity responses, which in turn mutes the clear-sky radiative response and largely removes the HC weakening. This suggests an important pathway through which cloud radiative feedbacks modulate clear-sky radiative feedbacks.

The dominant role of the cold patch in shaping the basin-wide radiative response is notable, given that the western Pacific warm pool is commonly considered central to global radiative feedbacks through its influence on free tropospheric temperature over the eastern equatorial Pacific (Zhou et al. 2016; Dong et al. 2019). Our results from a coupled perspective suggest that eastern Pacific cooling can exert a disproportionate influence on tropical convective organization, offering a view distinct from the conventional fixed-SST perspective that emphasizes the central role of warm-pool convection. Furthermore, the convective pattern generated by the cold patch closely resembles the observed ITCZ structure, despite the highly idealized nature of our model, which lacks both land and a dynamical ocean. This suggests that the equatorial Pacific convective pattern may be shaped, to first order, by the eastern Pacific cold tongue rather than by the western Pacific warm pool. This possibility will be explored in a subsequent study. Put together, our results highlight the importance of a cold eastern Pacific in shaping the large-scale circulation and radiative response of the tropical Pacific. This does not necessarily imply that the relevant forcing must be local to the eastern equatorial Pacific. Rather, remote forcings that perturb the eastern Pacific may also have broad climatic impacts. For example, Southern Ocean cooling that extends into the southeastern Pacific has been shown to control global radiative feedback in recent decades (Kang et al. 2023).

Strong cold-patch forcing reorganizes tropical convection in both zonal and meridional directions. Zonally, subsidence is enhanced over and west of the cold patch, corresponding to a WC strengthening. Meridionally, ascent is reduced within the equatorial band and enhanced in the adjacent off-equatorial regions, corresponding to a HC weakening. This spatial reorganization of deep convection can be understood from a convective-instability perspective (Williams and Pierrehumbert 2017; Zhang and Fueglistaler 2020), or equivalently visualized using the circus tent analogy (Williams et al. 2023). Cooling and drying driven by cold patch decrease the subcloud MSE, including over the warm patch region where deep convection originally occurs. This reduction in subcloud MSE over deep convection regions, in turn, lowers the free-tropospheric saturation MSE throughout the deep tropics between 20°S and 20°N. Over the equatorial region, the reduction in subcloud MSE exceeds the reduction in free-tropospheric saturation MSE, thereby suppressing deep convection. In contrast, in the off-equatorial region, the reduction in free-tropospheric saturation MSE dominates, making these regions relatively more favorable for deep convection. As a result, ascent shifts away from the equatorial band toward the off-equatorial tropics, indicative of a weakened HC. Because this mechanism depends critically on the spatial structure of the SST response, the convective-instability index provides a more useful indicator of convective reorganization than the energy flux potential, which does not explicitly account for SST changes.

We note that, for our study, the idealized aquaplanet slab ocean configuration is essential because it allows us to systematically control the WC strength by the applied Q_{WC} flux, thereby isolating the HC response to variations in WC strength. As a direct consequence, however, this setup excludes several key features of the real climate system. For example, ocean dynamics are known to damp the effects of prescribed Q-flux perturbation (Green and Marshall 2017; Kang et al. 2018). This effect is particularly pronounced over the eastern Pacific cold tongue region, where the damping is stronger than over the western Pacific warm pool (Park et al. 2022). The asymmetry between the cold- and warm-patch responses may therefore be overestimated in our configuration. Nevertheless, fully coupled model experiments also shows that heat perturbations over the eastern equatorial Pacific elicit stronger and more far-reaching response than comparable perturbations over the western equatorial Pacific (Park et al. 2022), suggesting that the qualitative asymmetry identified here is not an artifact of the slab ocean configuration.

Overall, our findings highlight the importance of the cold-patch dynamics in coupling the Walker and Hadley circulations and in shaping tropical convective patterns more broadly. While much of the existing literature has emphasized the central role of western Pacific warm pool in shaping tropical convection and radiative feedbacks, our results shed new light on the underappreciated influence of the eastern Pacific cold tongue, particularly through its ability to trigger low cloud radiative feedbacks. This study offers an alternative conceptual view of tropical Pacific atmospheric dynamics, one in which the eastern Pacific cold tongue plays an active role in organizing tropical convection and mediating interactions between the Walker and Hadley circulations.

Acknowledgments.

We thank Moritz Günther for providing a thorough internal review of the initial manuscript at the Max Planck Institute for Meteorology. We also thank Hauke Schmidt and Moritz Günther for fruitful discussions, and Thomas Raddatz for technical support with the model experiments.

Data Availability Statement.

The Max Planck Earth system model MPI-ESM1.2 is subject to the Custom Data set Terms detailed at Model Development Team Max-Planck-Institut für Meteorologie (2024). The source code version we used in this study as well as the scripts for preprocessing, model execution, postprocessing and analysis of the results are available from Edmond, the Open Research Data Repository for the Max Planck Society (Schimmer 2026). Data for this study is subject to the terms of the Creative Commons Attribution 4.0 International (CC BY 4.0) license and will be uploaded to the German Climate Computing Center (DKRZ) long-term archive for documentation after review.

REFERENCES

Andrews, T., and M. J. Webb, 2018: The Dependence of Global Cloud and Lapse Rate Feedbacks on the Spatial Structure of Tropical Pacific Warming. *J. Climate*, **31**, 641–654, https://doi.org/10.1175/JCLI-D-17-0087.1.

Barichivich, J., E. Gloor, P. Peylin, R. J. W. Brienen, J. Schöngart, J. C. Espinoza, and K. C. Pattnayak, 2018: Recent intensification of Amazon flooding extremes driven by strengthened Walker circulation. *Sci. Adv.*, **4**, eaat8785, https://doi.org/10.1126/sciadv.aat8785.

Betts, A. K., 1982: Saturation point analysis of moist convective overturning. *J. Atmos. Sci.*, **39**, 1484-1505. https://doi.org/10.1175/1520-0469(1982)039<1484:SPAOMC>2.0.CO;2

Bischoff, T., and T. Schneider, 2016: The Equatorial Energy Balance, ITCZ Position, and Double-ITCZ Bifurcations. *J. Climate*, **29**, 2997–3013, https://doi.org/10.1175/JCLI-D-15-0328.1.

Bjerknes J., 1969: Atmospheric teleconnections from the equatorial Pacific. *Mon. Wea. Rev.*, **97**, 163–172, doi:10.1175/ 1520-0493(1969)097,0163:ATFTEP.2.3.CO;2.

Boos, W. R., and R. L. Korty, 2016: Regional energy budget control of the intertropical convergence zone and application to mid-Holocene rainfall. *Nat. Geosci.*, **9**, 892–897, https://doi.org/10.1038/ngeo2833.

Bordoni, S., and T. Schneider, 2008: Monsoons as eddy-mediated regime transitions of the tropical overturning circulation. *Nat. Geosci.*, **1**, 515–519, https://doi.org/10.1038/ngeo248.

Bretherton, C. S., and A. H. Sobel, 2002: A Simple Model of a Convectively Coupled Walker Circulation Using the Weak Temperature Gradient Approximation. *J. Climate*, **15**, 2907–2920, https://doi.org/10.1175/1520-0442(2002)015%253C2907:ASMOAC%253E2.0.CO;2.

——, and P. K. Smolarkiewicz, 1989: Gravity Waves, Compensating Subsidence and Detrainment around Cumulus Clouds. *J. Atmos. Sci.*, **46**, 740-759

Chemke, R., and J. Yuval, 2023: Human-induced weakening of the Northern Hemisphere tropical circulation. *Nature*, **617**, 529–532. https://doi.org/10.1038/s41586-023-05903-1

Dong, Y., C. Proistosescu, K. C. Armour, and D. S. Battisti, 2019: Attributing Historical and Future Evolution of Radiative Feedbacks to Regional Warming Patterns using a Green's Function Approach: The Preeminence of the Western Pacific. *J. Climate*, **32**, 5471–5491, https://doi.org/10.1175/JCLI-D-18-0843.1.

Duffy, M. L., and P. A. O'Gorman, 2023: Intermodel Spread in Walker Circulation Responses Linked to Spread in Moist Stability and Radiation Responses. *J. Geophys. Res. Atmos.*, **128**, e2022JD037382, https://doi.org/10.1029/2022JD037382.

Emanuel, K., 2007: Quasi-equilibrium dynamics of the tropical atmosphere. *The global circulation of the atmosphere*, T. Schneider and A. H. Sobel, Eds., Princeton University Press, 186-218.

Fan, C.-S., and D. Dommenget, 2021: A diagnostic model for the large-scale tropical circulation based on moist static energy balance. *Climate. Dyn.*, **57**, 3159–3181, https://doi.org/10.1007/s00382-021-05861-2.

Fedorov, A. V., N. J. Burls, K. T. Lawrence, and L. C. Peterson, 2015: Tightly linked zonal and meridional sea surface temperature gradients over the past five million years. *Nat. Geosci.*, **8**, 975–980, https://doi.org/10.1038/ngeo2577.

Feldl, N., and S. Bordoni, 2016: Characterizing the Hadley Circulation Response through Regional Climate Feedbacks. *J. Climate*, **29**, 613–622, https://doi.org/10.1175/JCLI-D-15-0424.1.

——, D. M. W. Frierson, and G. H. Roe, 2014: The influence of regional feedbacks on circulation sensitivity. *Geophys. Res. Lett.*, **41**, 2212–2220, https://doi.org/10.1002/2014GL059336.

Feng, J., J. Li, F. Jin, Z. Liu, X. Nan, and Y. Guo, 2016: Contrasting Responses of the Hadley Circulation to Equatorially Asymmetric and Symmetric Meridional Sea Surface Temperature Structures. *J. Climate*, **29**, 8949–8963, https://doi.org/10.1175/JCLI-D-16-0171.1.

Green, B., and J. Marshall, 2017: Coupling of Trade Winds with Ocean Circulation Damps ITCZ Shifts. *J. Climate*, **30**, 4395–4411, https://doi.org/10.1175/JCLI-D-16-0818.1.

Guo, Y., and Z. Tan, 2018: On the Sensitivity of the Relationship Between Hadley Circulation Asymmetry and ENSO in CMIP5 Models. *Geophys. Res. Lett.*, **45**, 9253–9259, https://doi.org/10.1029/2018GL079515.

Hartmann, D. L., 2022: The Antarctic ozone hole and the pattern effect on climate sensitivity. *Proc. Natl. Acad. Sci. U.S.A.*, **119**, e2207889119, https://doi.org/10.1073/pnas.2207889119.

Held, I. M., and A. Y. Hou, 1980: Nonlinear axially symmetric circulations in a nearly inviscid atmosphere. *J. Atmos. Sci.*, **37**, 515–533, doi:10.1175/1520-0469(1980)037,0515: NASCIA.2.0.CO;2.

Hersbach, H., and Coauthors, 2020: The ERA5 global reanalysis. *Quart. J. Roy. Meteor. Soc.*, **146**, 1999–2049, https://doi.org/10.1002/qj.3803.

Hu, Y., H. Huang, and C. Zhou, 2018: Widening and weakening of the Hadley circulation under global warming. *Sci. Bull.*, **63**, 640–644, https://doi.org/10.1016/j.scib.2018.04.020.

Hwang, Y., S. Xie, C. Deser, and S. M. Kang, 2017: Connecting tropical climate change with Southern Ocean heat uptake. *Geophys. Res. Lett.*, **44**, 9449–9457, https://doi.org/10.1002/2017GL074972.

Kang, S. M., I. M. Held, D. M. W. Frierson, and M. Zhao, 2008: The Response of the ITCZ to Extratropical Thermal Forcing: Idealized Slab-Ocean Experiments with a GCM. *J. Climate*, **21**, 3521–3532, https://doi.org/10.1175/2007JCLI2146.1.

——, Y. Shin, and S.-P. Xie, 2018: Extratropical forcing and tropical rainfall distribution: energetics framework and ocean Ekman advection. *npj Clim. Atmos. Sci.*, **1**, 20172, https://doi.org/10.1038/s41612-017-0004-6.

——, S.-P. Xie, Y. Shin, H. Kim, Y.-T. Hwang, M. F. Stuecker, B. Xiang, and M. Hawcroft, 2020: Walker circulation response to extratropical radiative forcing. *Sci. Adv.*, **6**, eabd3021, https://doi.org/10.1126/sciadv.abd3021.

——, Y. Yu, C. Deser, X. Zhang, I.-S. Kang, S.-S. Lee, K. B. Rodgers, and P. Ceppi, 2023: Global impacts of recent Southern Ocean cooling. *Proc. Natl. Acad. Sci. U.S.A.*, **120**, e2300881120, https://doi.org/10.1073/pnas.2300881120.

——, M. Watanabe, and V. Gayler, 2025: Common and Distinct Drivers of Convective Mass Flux and Walker Circulation Changes. *Geophys. Res. Lett.*, **52**, e2024GL111897, https://doi.org/10.1029/2024GL111897.

Kim, D., H. Kim, S. M. Kang, M. F. Stuecker, and T. M. Merlis, 2022: Weak Hadley cell intensity changes due to compensating effects of tropical and extratropical radiative forcing. *npj Clim. Atmos. Sci.*, **5**, 61, https://doi.org/10.1038/s41612-022-00287-x.

Korty, R. L., and T. Schneider, 2008: Extent of Hadley circulations in dry atmospheres. *Geophys. Res. Lett.*, **35**, 2008GL035847, https://doi.org/10.1029/2008GL035847.

Kosaka, Y., and S.-P. Xie, 2013: Recent global-warming hiatus tied to equatorial Pacific surface cooling. *Nature*, **501**, 403–407, https://doi.org/10.1038/nature12534.

Kosovelj, K., and Ž. Zaplotnik, 2023: Indices of Pacific Walker Circulation Strength. *Atmosphere*, **14**, 397, https://doi.org/10.3390/atmos14020397.

Lu, J., G. Chen, and D. M. W. Frierson, 2008: Response of the Zonal Mean Atmospheric Circulation to El Niño versus Global Warming. *J. Climate*, **21**, 5835–5851, https://doi.org/10.1175/2008JCLI2200.1.

Ma, J., and J. Li, 2008: The principal modes of variability of the boreal winter Hadley cell. *Geophys. Res. Lett.*, **35**, 2007GL031883, https://doi.org/10.1029/2007GL031883.

Merlis, T. M., and T. Schneider, 2011: Changes in Zonal Surface Temperature Gradients and Walker Circulations in a Wide Range of Climates. *J. Climate*, **24**, 4757–4768, https://doi.org/10.1175/2011JCLI4042.1.

Model Development Team Max-Planck-Institut für Meterologie. 2024: MPI-ESM 1.2.01p7. Edmond, accessed 25 August 2026, https://doi.org/10.17617/3.H44EN5

Neelin, J. D., and I. M. Held, 1987: Modeling Tropical Convergence Based on the Moist Static Energy Budget. *Mon. Wea. Rev.*, **115**, 3–12, https://doi.org/10.1175/1520-0493(1987)115%253C0003:MTCBOT%253E2.0.CO;2.

Park, C., S. M. Kang, M. F. Stuecker, and F. Jin, 2022: Distinct Surface Warming Response Over the Western and Eastern Equatorial Pacific to Radiative Forcing. *Geophys. Res. Lett.*, **49**, e2021GL095829, https://doi.org/10.1029/2021GL095829.

Pikovnik, M., Ž. Zaplotnik, L. Boljka, and N. Žagar, 2022: Metrics of the Hadley circulation strength and associated circulation trends. *Wea. Climate Dyn.*, **3**, 625–644, https://doi.org/10.5194/wcd-3-625-2022.

Raymond, D. J., 1995: Regulation of moist convection over the west Pacific warm pool. *J. Atmos. Sci.*, **52**, 3945-3959. https://doi.org/10.1175/1520-0469(1995)052<3945:ROMCOT>2.0.CO;2

Schimmer, R. 2026: MPIESM-1.2 model version and scripts used to examine Walker and Hadley circulation changes. Edmond, accessed 25 August 2026. https://doi.org/10.17617/3.PV5AZI

Schwendike, J., P. Govekar, M. J. Reeder, R. Wardle, G. J. Berry, and C. Jakob, 2014: Local partitioning of the overturning circulation in the tropics and the connection to the Hadley and Walker circulations. *J. Geophys. Res. Atmos.*, **119**, 1322–1339, https://doi.org/10.1002/2013JD020742.

Sobel, A. H., J. Nilsson, and L. M. Polvani, 2001: The Weak Temperature Gradient Approximation and Balanced Tropical Moisture Waves*. *J. Atmos. Sci.*, **58**, 3650–3665, https://doi.org/10.1175/1520-0469(2001)058%253C3650:TWTGAA%253E2.0.CO;2.

Stevens, B., and Coauthors, 2013: Atmospheric component of the MPI-M Earth System Model: ECHAM6. *J. Adv. Model Earth Syst.*, **5**, 146–172, https://doi.org/10.1002/jame.20015.

Sud, Y. C., G. K. Walker, and K. -M. Lau, 1999: Mechanisms regulating sea-surface temperatures and deep convection in the tropics. *Geophys. Res. Lett.*, **26**, 1019–1022, https://doi.org/10.1029/1999GL900197.

Sun, D., and K. E. Trenberth, 1998: Coordinated heat removal from the equatorial Pacific during the 1986–87 El Niño. *Geophys. Res. Lett.*, **25**, 2659–2662, https://doi.org/10.1029/98GL01813.

Takahashi, K., and D. S. Battisti, 2007: Processes Controlling the Mean Tropical Pacific Precipitation Pattern. Part I: The Andes and the Eastern Pacific ITCZ. *J. Climate*, **20**, 3434–3451, https://doi.org/10.1175/JCLI4198.1.

Trenberth, K. E., and D. P. Stepaniak, 2003: Covariability of Components of Poleward Atmospheric Energy Transports on Seasonal and Interannual Timescales. *J. Climate*, **16**, 3691–3705, https://doi.org/10.1175/1520-0442(2003)016%253C3691:COCOPA%253E2.0.CO;2.

Tseng, H., and Y. Hwang, 2024: Contrasting the Evolution of the Tropical Pacific SST Responses to Time-Invariant Extratropical Forcings in the Two Hemispheres. *Geophys. Res. Lett.*, **51**, e2024GL110551, https://doi.org/10.1029/2024GL110551.

Voigt, A., and T. A. Shaw, 2015: Circulation response to warming shaped by radiative changes of clouds and water vapour. *Nat. Geosci.*, **8**, 102–106, https://doi.org/10.1038/ngeo2345.

Watanabe, M., T. Iwakiri, Y. Dong, and S. M. Kang, 2023: Two Competing Drivers of the Recent Walker Circulation Trend. *Geophys. Res. Lett.*, **50**, e2023GL105332, https://doi.org/10.1029/2023GL105332.

Williams, A. I. L., N. Jeevanjee, and J. Bloch-Johnson, 2023: Circus Tents, Convective Thresholds, and the Non-Linear Climate Response to Tropical SSTs. *Geophys. Res. Lett.*, **50**, e2022GL101499, https://doi.org/10.1029/2022GL101499.

Williams, I. N., and R. T. Pierrehumbert, 2017: Observational evidence against strongly stabilizing tropical cloud feedbacks. *Geophys. Res. Lett.*, **44**, 1503–1510, https://doi.org/10.1002/2016GL072202.

Wills, R. C., X. J. Levine, and T. Schneider, 2017: Local Energetic Constraints on Walker Circulation Strength. *J. Atmos.c Sci.*, **74**, 1907–1922, https://doi.org/10.1175/JAS-D-16-0219.1.

Wills, R. C. J., Y. Dong, C. Proistosecu, K. C. Armour, and D. S. Battisti, 2022: Systematic Climate Model Biases in the Large-Scale Patterns of Recent Sea-Surface Temperature and Sea-Level Pressure Change. *Geophys. Res. Lett.*, **49**, e2022GL100011, https://doi.org/10.1029/2022GL100011.

Wood, R., and C. S. Bretherton, 2006: On the Relationship between Stratiform Low Cloud Cover and Lower-Tropospheric Stability. *J. Climate*, **19**, 6425–6432, https://doi.org/10.1175/JCLI3988.1.

Zhang, Y., and S. Fueglistaler, 2020: How Tropical Convection Couples High Moist Static Energy Over Land and Ocean. *Geophys. Res. Lett.*, **47**, e2019GL086387, https://doi.org/10.1029/2019GL086387.

Zhou, C., M. D. Zelinka, and S. A. Klein, 2016: Impact of decadal cloud variations on the Earth’s energy budget. *Nat. Geosci.*, **9**, 871–874, https://doi.org/10.1038/ngeo2828.

Journal of Climate

Supporting Information for

Coupling between Walker and Hadley circulations mediated by low cloud feedback

Rolf Schimmer,[a,b] Sarah M. Kang[a]

[a] *Max Planck Institute for Meteorology, Bundesstraße 53, 20146 Hamburg, Germany.*

[b] *International Max Planck Research School on Earth System Modelling, Bundesstraße 53, 20146 Hamburg, Germany.*

Contents of this file

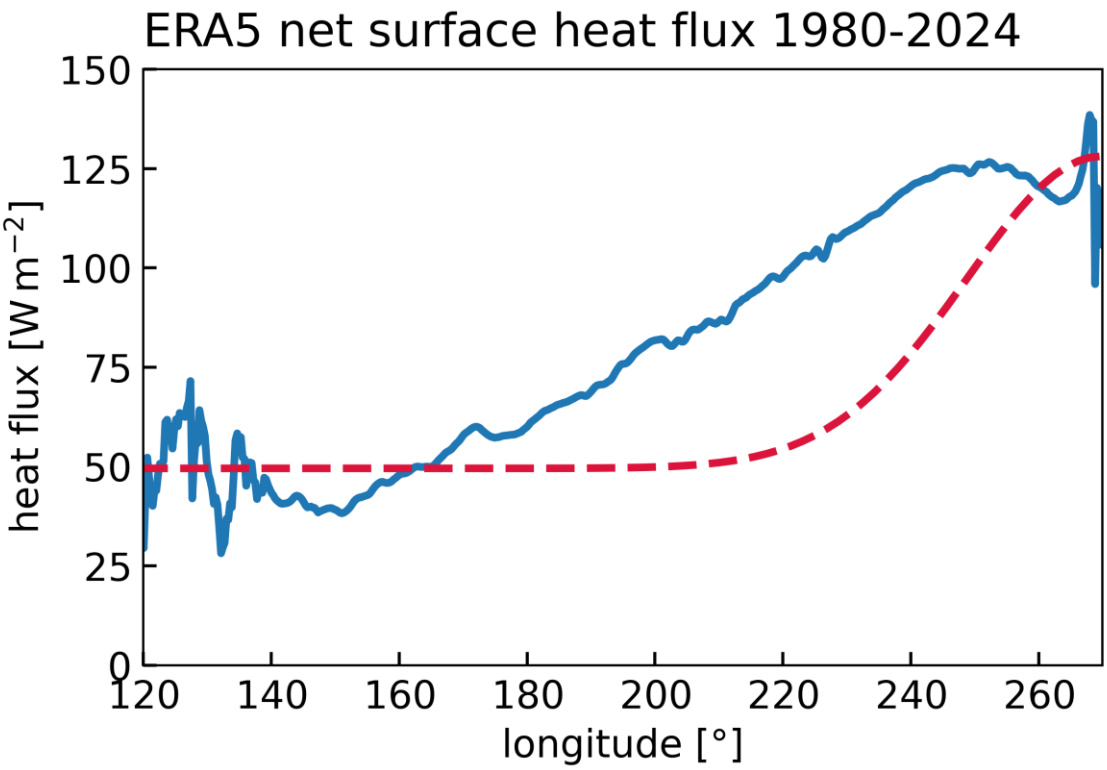

Fig. S1. Net surface heat flux across the Pacific averaged between 2°S and 2°N based on the ERA5 reanalysis data from 1980 to 2024 (blue). The zonal gradient in net surface heat flux is approximately 90 W m^{-2}. Overlayed in red is the aquaplanet slab ocean experiment with a prescribed cold-patch-only heat flux of $Q_1 = 80$ W m^{-2}.

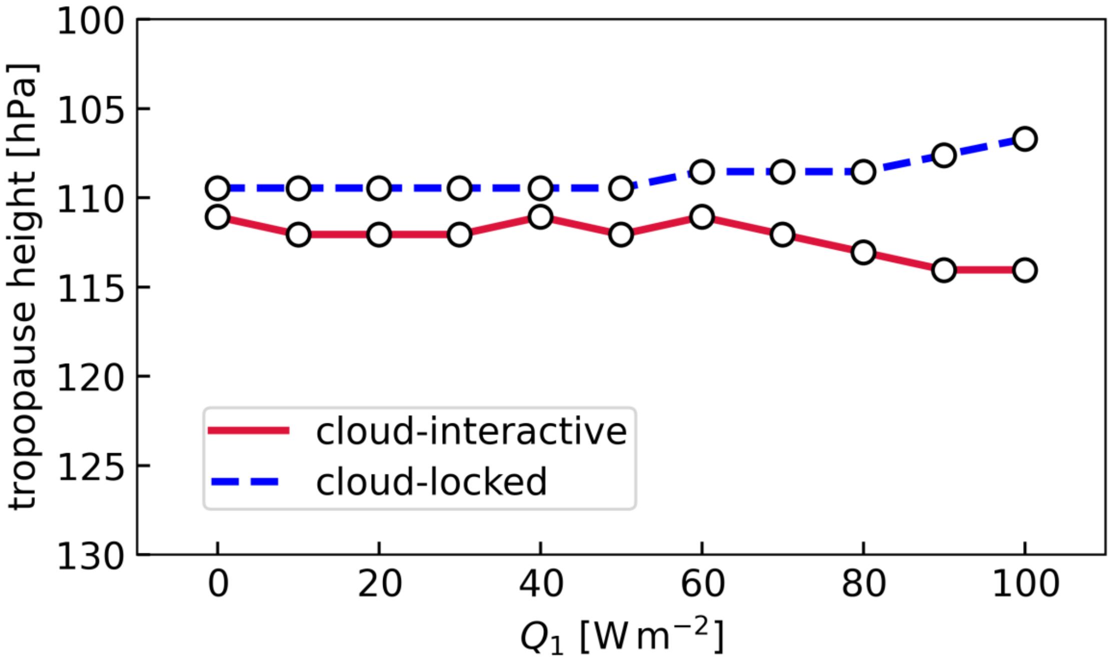

Fig. S2. Tropopause height in hPa for the cloud-interactive (red) and cloud-locked (blue dashed) cases. The tropopause height is defined by the lowest level at which the lapse rate ≥ −2 K km^{-1}. The lapse rate is computed based on the temperature averaged between 20°S and 20°N.

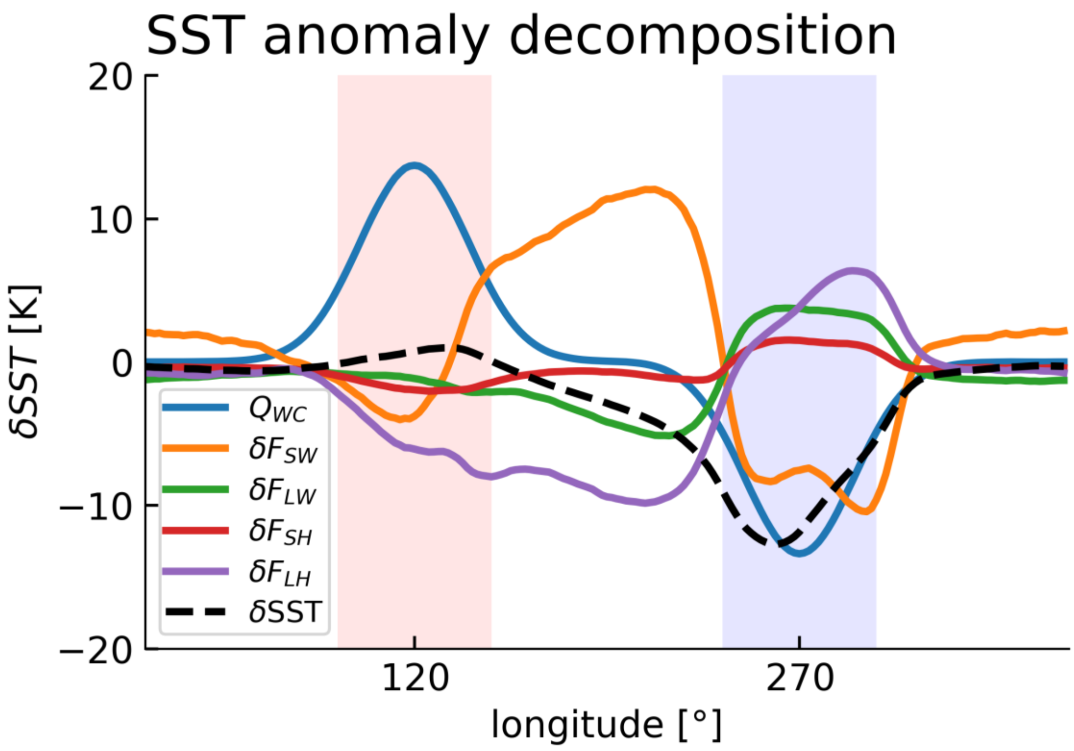

Fig. S3. Equatorial mean (φ ≤ ±5°) longitudinal profile of SST anomaly (black dashed), decomposed into contributions from prescribed Q_{WC} forcing (blue), shortwave radiation (orange), longwave radiation (green), sensible heat flux (red), and latent heat flux (purple), for the strong Q_{WC} case ($Q_1 = 100$ W m^{-2}). The analysis follows the anomalous SST decomposition method based on surface energy budget of Zhang et al. (2021).